This circulation uncertainty also has important implications for regional climate change. For example, CMIP models project, on average, a decrease of ~25% of Mediterranean precipitation by the end of the twenty-first century relative to the present day in the multimodel mean (Giorgi and Lionello 2008; Kelley et al. 2012; Polade et al. 2017; Tuel and Eltahir 2020; Garfinkel et al. 2020a). However, there is a wide spread among models participating in the fifth phase of CMIP (CMIP5), with projections ranging from essentially no change to over a 60% precipitation reduction over the eastern Mediterranean (Zappa et al. 2015; Polade et al. 2017; Garfinkel et al. 2020a). The uncertainty in circulation changes is a more important contributor to this uncertainty in future changes in precipitation and the hydrological cycle than the direct thermodynamic response to rising GHG (Elbaum et al. 2022). A better understanding of the processes that lead to diversity in the dynamical response to increased GHG is urgently needed.

Climate models cannot yet be run for centennial time scales at resolutions that explicitly resolve convection. Hence, models parameterize convection in order to represent known physical processes that lead to precipitation. These convection parameterizations are still a work in progress and are constantly being upgraded (Rio et al. 2019; Bartana et al. 2022; Lin et al. 2022). This raises the possibility that model uncertainty in the representation of convection (which may be reducible) is contributing to spread in the projected midlatitude circulation response to increased GHG, as pointed out by Fuchs et al. (2022) and Ghosh et al. (2024). Further, previous work using mechanism denial experiments has highlighted that the poleward shift is related to moist processes (Tan and Shaw 2020).

This study demonstrates that changing the convective parameterization in a single atmospheric general circulation model can lead to sharply diverging midlatitude circulation responses to increased GHG, and then aims to explain why the response is so sensitive. After introducing the model and data used in section 2, we demonstrate in section 3 that the settings used for the convection scheme have a leading-order impact on the circulation response, with a poleward shift evident only for some settings. Next, we evaluate which mechanisms appear capable of distinguishing between runs with and without a poleward shift (sections 4 and 5). We conclude with a summary and a discussion of the implications for subtropical precipitation and for model uncertainty across CMIP.

2. Data and methods

a. CMIP6 data

Thirteen CMIP6 models archive the vertically, latitudinally, and monthly resolved total diabatic heating (tntmp) for the preindustrial control and 4xCO_2 runs, and for reasons explained later in this manuscript, this output is crucial for understanding the diversity of jet shifts in response to increased greenhouse gases. These 13 CMIP6 models are the same models used by Lachmy (2022), and they are listed in Table 1 of Lachmy (2022). Note that of these 13 models, only eight provide the separate tendencies due to radiation (tntr), latent heating (tntc), and boundary layer mixing (tntscpbl), and of these eight, the sum equals the total heating only for four. Since the individual diabatic terms are available for so few models to begin with and the budget is closed for an even smaller subset, we do not use the individual terms when considering CMIP6 output.

b. A model of an idealized moist atmosphere (MiMA)

We use the Model of an Idealized Moist Atmosphere (MiMA) introduced by Jucker and Gerber (2017) and Garfinkel et al. (2020b,c). This model builds on the aquaplanet models of Frierson et al. (2006, 2007), and Merlis et al. (2013). Very briefly, the model solves the moist primitive equations on the sphere, employing a simplified Betts–Miller convection scheme (Betts 1986; Betts and Miller 1986; Frierson 2007), an idealized boundary layer scheme based on Monin–Obukhov similarity theory, and a purely thermodynamic (or slab) ocean. An important feature for this paper is that we use a realistic radiation scheme Rapid Radiative Transfer Model (RRTMG; Mlawer et al. 1997; Iacono et al. 2000), which allows us to explicitly simulate the radiative response to water vapor (Tan et al. 2019). Please see Jucker and Gerber (2017) for more details. All simulations in this paper are run in an aquaplanet configuration with none of the building blocks of stationary waves developed by Garfinkel et al. (2020b,c). There are no clouds in our model, and hence mechanisms for a poleward shift involving cloud radiative effects are, by construction, not in operation and cannot be assessed. The role of a dynamic ocean for circulation shifts (e.g., Nakamura et al. 2004; Okajima et al. 2018) cannot be assessed in this configuration either.

c. Convection scheme

The simplified Betts–Miller convection scheme (Betts 1986; Betts and Miller 1986; Frierson 2007) contains one key parameter and two flags that modify the parameterization, and we explore their importance for future jet and storm track changes in this work:

1) RHrelax: This parameter determines how effectively convection stabilizes the atmospheric column if convection is triggered at any location and time step. RHrelax specifies the relative humidity of the atmospheric profile to which the scheme relaxes temperature and humidity to remove convective instability (see Frierson 2007, section 2d therein, for further details). In this study it is varied from 0.6 to 0.85. A lower value of RHrelax allows the convection scheme to produce more precipitation and more efficiently stabilize the atmospheric column. This parameter is called “rhbm” in the model’s namelist.
2) shallow_convection(on/off): This flag toggles the use of a simple parameterization of shallow convection designed to capture the moisture and temperature effects of trade cumulus (radiative effects of all cloud types are not included in any configuration). Trade cumulus are formed from shallow convection that does not lead to net precipitation but nonetheless moisten and warm the midtroposphere.

   If the Betts–Miller scheme finds that moisture relaxation would lead to a net moistening of the profile (which can

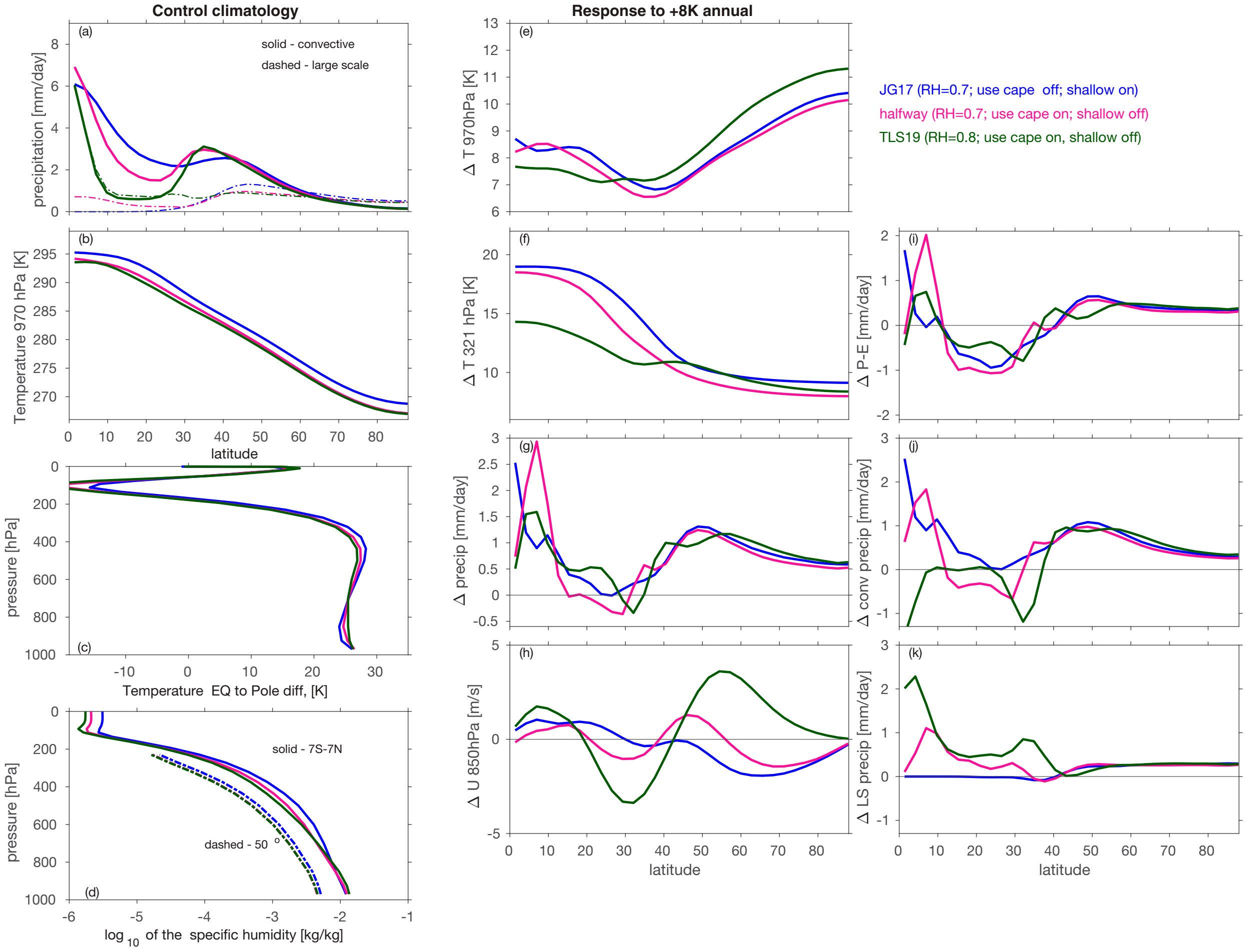

FIG. 1. (left) Climatology in the present-day simulation for each configuration of (a) precipitation, (b) temperature at 970 hPa, (c) equator-to-pole temperature difference as a function of level, and (d) specific humidity at the equator and at 50°. (center),(right) The response to ~8 K warming of (e) lower-tropospheric temperature, (f) upper-tropospheric temperature, (g) precipitation, (h) lower-tropospheric zonal-mean wind, (i) precipitation minus evaporation, (j) convection precipitation, and (k) large-scale precipitation. One halfway simulation is included as well to focus on the relative importance of shallow convection and RHrelax, while others are excluded for visual clarity.

The resulting climatological distribution of 970-hPa temperature is shown in Fig. 1b. All configurations simulate a similar equator-to-pole temperature difference, with the maximum temperature gradient in midlatitudes. The difference in temperature between the tropics (equatorward of 10°) and pole (latitudes exceeding 80°) is shown for each pressure level in Fig. 1c: it is clear that the different configurations simulate a similar climatology by this metric. The vertical profile of equatorial specific humidity is shown in Fig. 1d. The simulations with shallow convection on (e.g., JG17) simulate a moister mid- and upper troposphere (and also stratosphere), than the simulations with shallow convection off (e.g., TLS19). In contrast, tropical boundary layer moisture is larger in TLS19 than in JG17, also consistent with the settings for shallow convection. A higher value of RHrelax leads to more moisture at all levels if shallow convection is on, as the convection scheme removes less moisture from the atmosphere, and use_CAPE has a smaller impact on the climatology than either of the other two parameters (Fig. S1 in the online supplemental material).

Figures 2a and 2b shows the temperature change for each configuration in response to increased CO$_2$ (ΔT, where Δ refers to the response to increased GHGs computed by differencing the present-day and +8 K simulations); similar plots for the halfway simulations are shown in supplemental Fig. 1. All global warming simulations project enhanced warming of the tropical upper troposphere and polar amplification, similar to that projected in CMIP models. Polar amplification is seen more clearly in Fig. 1e, which shows the 970 hPa ΔT in each configuration. The enhanced warming in the tropical upper troposphere is seen more explicitly in Fig. 1f, which shows the ΔT at 321 hPa in each configuration. This temperature change leads to increased static stability in both configurations in most of the troposphere (Figs. 2c,d).

The absolute atmospheric moisture content increases in all configurations (Figs. 2e,f; see also supplemental Fig. 1) as

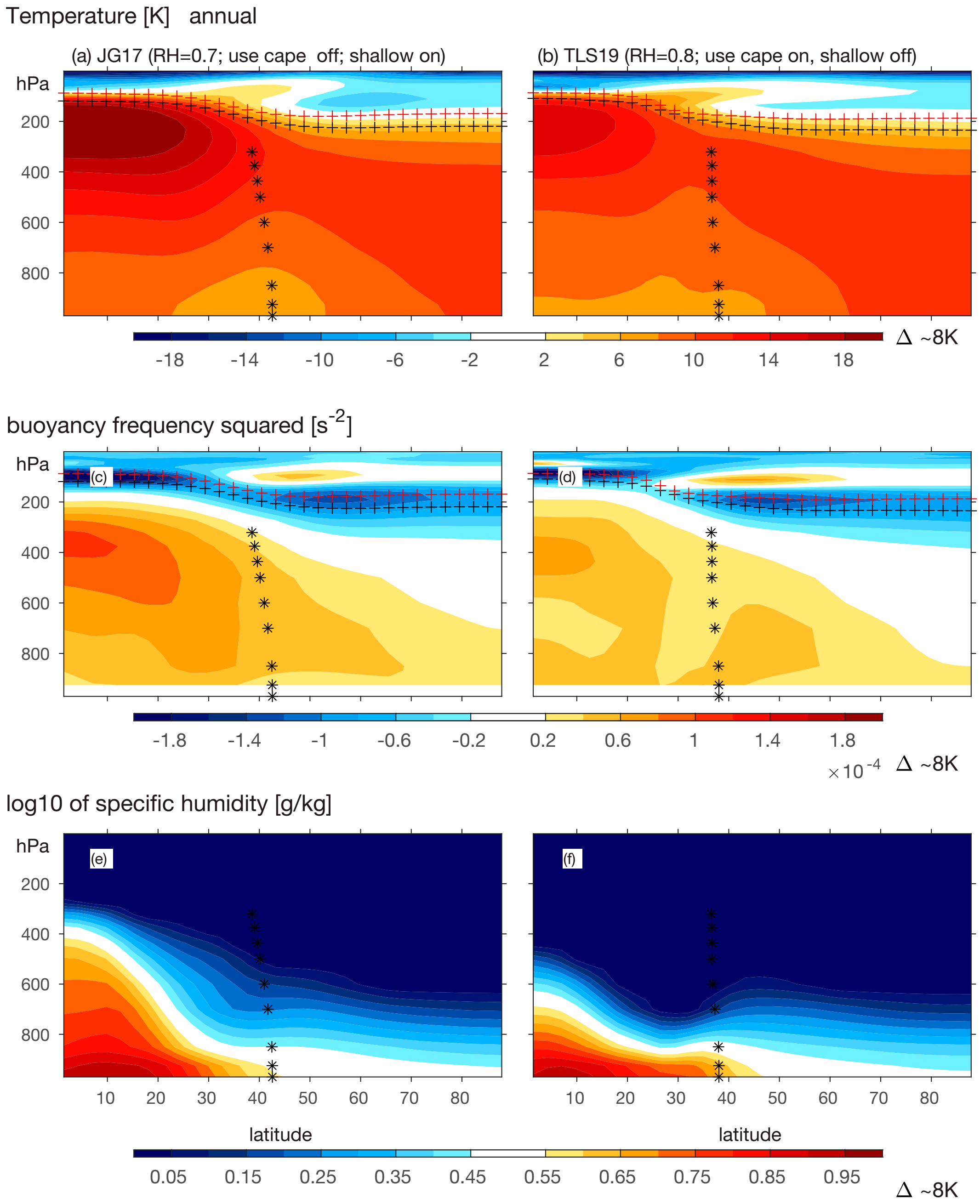

FIG. 2. Difference in latitude vs pressure (a),(b) temperature, (c),(d) buoyancy frequency, and (e),(f) specific humidity between an ∼8-K warming integration and a 1xCO_2 integration for the different aquaplanet configurations. Asterisks denote the climatological jet latitude. Black and red plus signs denote the tropopause using the WMO -2 K km^{-1} definition for the present day and increased GHG simulations, respectively.

expected from the Clausius–Clapeyron relation (Held and Soden 2006). The precipitation response in each simulation is similar in a general sense (Fig. 1g), with an increase in the tropics and midlatitudes and a near-zero or weak reduction in the subtropics. Despite this overall similarity, there are important differences among the configurations: for example, the latitude in which subtropical precipitation decreases is near 33° for TLS19 but near 25° for JG17. Such uncertainty is of great importance to areas with Mediterranean climates, in which much of the rain falls from the equatorward edge of the wintertime storm track (Seager et al. 2019), an issue we return to in section 6. The TLS19 and JG17 configurations also differ as to the region where net aridification, as diagnosed by precipitation minus evaporation, becomes most severe (Fig. 1i).

These differences in the hydrological cycle response to global warming despite an essentially identical global mean warming motivate us to consider the circulation response for each configuration.

3. Sensitivity of the jet and storm track responses to the convection parameterization

We now consider the jet and storm track response to the increased GHG. Figures 3a and 3b show the zonal wind climatology (solid contours) and response to increased GHG (shading) for each configuration; similar figures for the halfway simulations are shown in supplemental Fig. 2). The jet latitude at each level is computed by fitting the zonal-mean zonal wind near the jet maxima (as computed at the model's T42 resolution of ∼3°) to a parabola, and then computing the maximum of the parabola at a meridional resolution of 0.12° (Garfinkel et al. 2013). All configurations feature a climatological near-surface westerly wind maximum near 40°. While the near-surface jet is 4° farther poleward in JG17, consistent with the effect of a shallow convection scheme on jet latitude in Fuchs et al. (2022), the climatological jet structure is a "merged jet" with the upper-tropospheric subtropical jet in all configurations, unlike the much larger differences associated with varied radiative assumptions in Tan et al. (2019).

In response to increased GHG, the subtropical jet accelerates in the upper troposphere in all configurations, consistent with CMIP models. The response of the near-surface jet, however, differs qualitatively among the configurations. For the JG17 configuration, the near-surface jet shifts slightly equatorward, as evidenced by the westerly anomaly equatorward of the jet maximum and easterly anomaly poleward of the jet maximum. In contrast, the near-surface jet shifts poleward for the TLS19 configuration, with an easterly anomaly on the equatorward jet flank and westerly anomaly on the poleward flank. The intermediate configurations, with only one of the differences between JG17 and TLS19 included, indicate that of the three parameters, shallow convection is the most important, RHrelax has a moderate effect, and use_CAPE has minimal importance (supplemental Fig. 2). Fuchs et al. (2022) also find a stronger poleward near-surface jet shift when shallow convection is turned off, as in TLS19. If we assume that each of the 37 years of integration is a unique degree of freedom (which is very conservative considering the *e*-folding time scales of the first empirical orthogonal function of near-surface zonal wind is less than 50 days), then the 95% error bars on the TLS19 jet shift are [3.9 4.7] while those on JG17 are [−0.9 0.2]. Hence the difference in jet shift is very robust.

Figure 1h summarizes the ΔU at 850 hPa for each configuration. For the TLS19 configuration (green), a clear dipole is present, with an easterly anomaly equatorward of 40° and a westerly anomaly poleward of 40°. An opposite response is evident in the JG17 configuration (blue).

Changes in the eddy kinetic energy ($\hat{u}^2 + \hat{v}^2$, where $\hat{x}$ denotes bandpass filtered x using a fifth-order Butterworth filter with cutoffs at 2 and 8 days; ΔEKE) are shown in Figs. 3c and 3d. In all configurations, the EKE decreases near and equatorward of its climatological maximum in the lower and midtroposphere, but increases near the tropopause and lower stratosphere. Both the upward expansion and the weakening on the equatorward flank are similar to that seen in CMIP models (e.g., Chang et al. 2012), and is likely due to a rising of the tropopause and to increased static stability. For the TLS19 configuration with a poleward jet shift, a slight strengthening of EKE is present on the poleward flank, consistent with the change evident in the Southern Hemisphere in CMIP models.

The poleward shifts (or lack thereof) in EKE and in the near-surface jet are tightly coupled. To demonstrate this, we define an index of storm track shift by taking the difference of pressure-weighted ΔEKE at 55° minus that at 30° (results are not sensitive to shifts of ∼5°, or to selecting specific pressure levels within the troposphere). We then contrast this index of the storm track shift (ordinate) with the change in jet latitude at 970 hPa (abscissa) for the TLS19, JG17, and halfway configurations in Fig. 4a. Configurations with a poleward jet shift also feature a relative strengthening of the storm track on its poleward flank as compared to its equatorward flank. Given the tight coupling between the near-surface jet and storm track as diagnosed by EKE, we treat them interchangeably in the rest of this paper. Specifically, all conclusions reached below with regards to the near-surface jet shift apply equally to the EKE shift as well. Additional metrics of the storm track will be discussed in section 4c.

These differences in the jet shift across the experiments are consistent with respective Δ eddy momentum flux (Figs. 5a,b): a dipole is evident for the TLS19 configuration with enhanced momentum flux poleward of its climatological position, acting to shift the jet poleward. In contrast, in the JG17 configuration, eddy momentum flux weakens at all latitudes in the upper troposphere (the upward shift associated with a rising tropopause will be discussed later).

4. Negating less-important mechanisms for the near-surface jet and storm track shift

The rest of this paper aims to understand which of the varied mechanisms listed in Shaw (2019) are capable of diagnosing why the near-surface jet (hereafter jet) and storm track shift poleward using the TLS19 settings for the convection parameterization, but not using the JG17 settings. We first demonstrate that many of the mechanisms reviewed by Shaw (2019) cannot be of leading-order importance for explaining the difference in jet shift in TLS19 versus in JG17, as their key physical process(es) respond at least as strongly in JG17 with an equatorward shift as compared to TLS19 with a poleward shift.

a. *Can temperature changes alone predict the shift?*

We first consider whether zonal-mean changes in the temperature structure of the atmosphere can account for the difference in jet shifts. The warming of the tropical upper troposphere in response to increased GHG has been argued to help induce the poleward jet shift (Butler et al. 2010) by a variety of distinct mechanisms detailed in Shaw (2019). If a warming of the tropical upper troposphere occurred only (or mainly) in simulations in which the jet shifted poleward, then we would be motivated

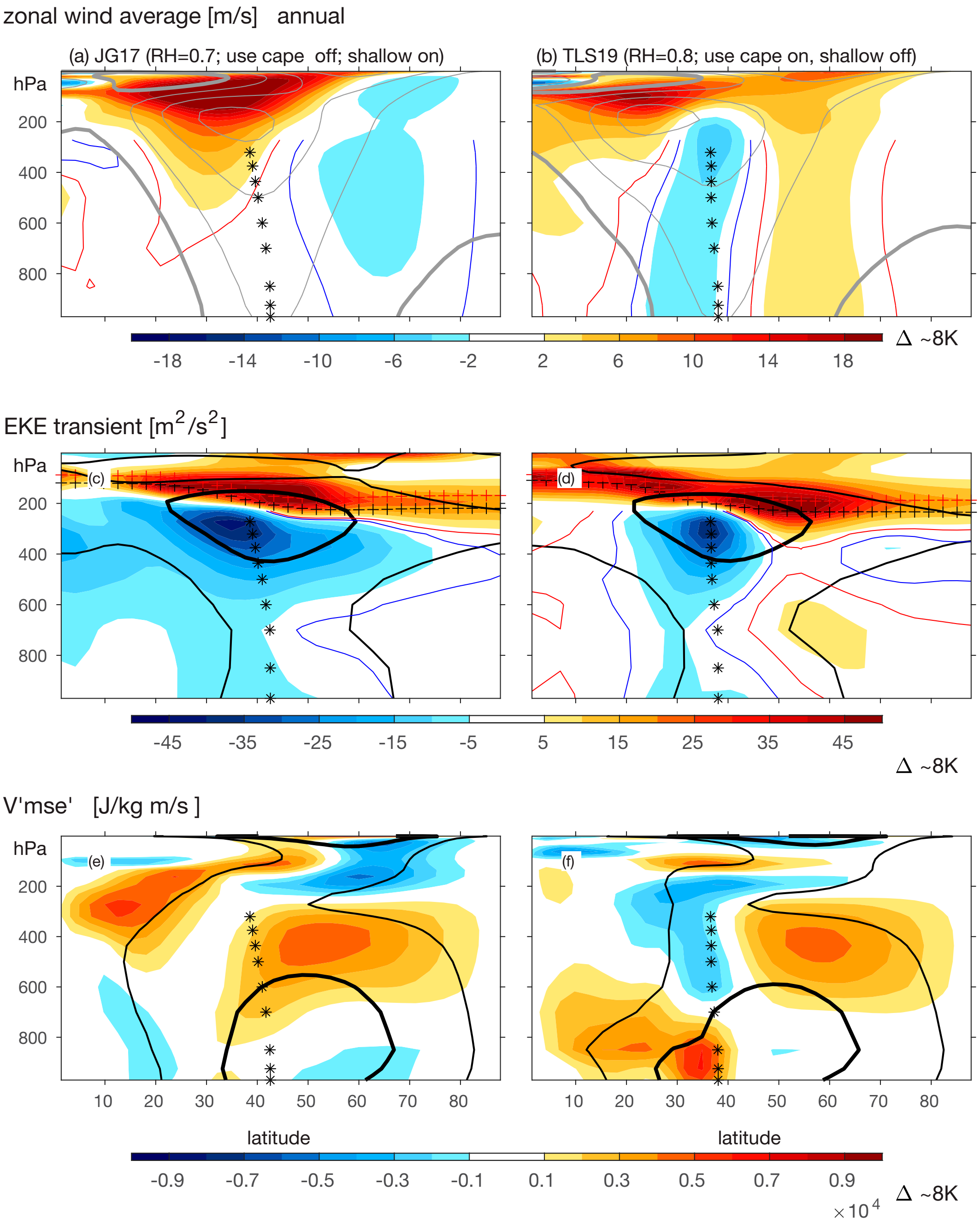

FIG. 3. Difference in latitude vs pressure (a),(b) zonal-mean zonal wind, (c),(d) transient (2–8-day band-passed) eddy kinetic energy, and (e),(f) poleward flux of moist static energy $\overline{v'\mathrm{mse}'}$ between an ~8 K warming integration and a 1xCO$_2$ integration (shaded contours), and the climatological profile in the 1xCO$_2$ run (black lines), for the different aquaplanet configurations. (top) Gray lines indicate the climatological profile in the 1xCO$_2$ run with a contour interval of 10 m s^{-1} and the zero line is thick, and the ±1 m s^{-1} contours of the response to increased GHG are indicated with thin red and blue lines. The climatological jet latitude is indicated with asterisks. (middle) Black and red plus signs denote the tropopause using the WMO −2 K km^{-1} definition for the present day and increased GHG simulations respectively, and the contours for the black lines are shown at ±30 and ±90 m^2 s^{-2}. The ±2 m^2 s^{-2} contours of the response to increased GHG are indicated with thin red and blue lines. (bottom) The contours for the black lines are at ±6000 and ±18 000 J kg m s^{-1}.

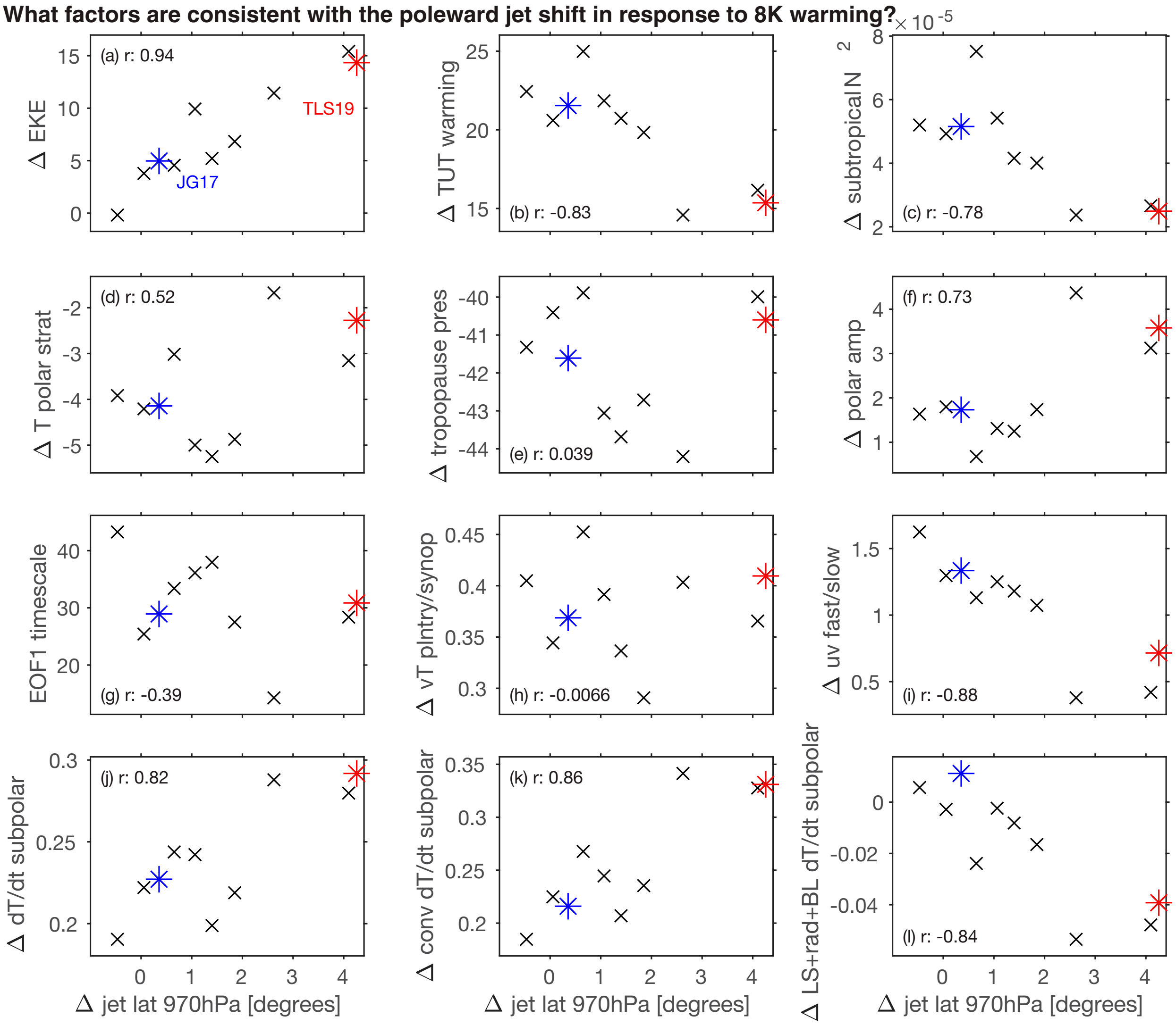

FIG. 4. Comparison of the jet shift at 970 hPa in all 10 configuration listed in Table 1 (abscissa) to (a) pressure-weighted ΔEKE at 55° minus that at 30°; (b) tropical upper-tropospheric warming, defined as the temperature change at 230 hPa from 5°S to 5°N; (c) subtropical static stability, defined as the change in the Brunt–Vaisala frequency at 321 hPa from 25° to 35°; (d) polar stratospheric cooling, defined as the temperature change at 112 hPa from 60° to the pole; (e) rising of the tropopause from 45° to 55°, computed by fitting the temperature profile for the grid points on either side of the −2 K km^{-1} threshold to a linear fit with 300 grid points, and finding the pressure at which the −2 K km^{-1} threshold is crossed; (f) polar amplification, defined as the temperature change at 970 hPa from 80° to the pole minus that from 5°S to 5°N; (g) synoptic eddy feedback, defined as the *e*-folding time scale of the first principal component time series computed following the methodology of Baldwin et al. (2003) and Gerber et al. (2008); (h) shift toward longer wavelengths, defined as the difference in $\overline{v'T'}$ at 700 hPa between wavenumber 1 and wavenumbers 5–7 from 35° to 55°; (i) shift toward faster phase speeds, defined as the difference in $\overline{u'v'}$ at 272 hPa between phase speeds of 20–30 m s^{-1} vs 3–10 m s^{-1} after area-weighting from the equator to the pole; (j) diabatic heating poleward of the jet, defined as the sum of all diabatic heating contributions (latent, radiative, and boundary layer) averaged from 450 to 775 hPa and 55° to 75° (see the rectangle on Fig. 9); (k) as in (j), but for the convective heating only; and (l) as in (j), but for the large-scale, radiative, and boundary layer heating only (total minus convective). The TLS19 and JG17 configurations are indicated with red and blue stars, and all others with × marks. All results are similar for ~10% changes in the level or latitudes chosen.

to examine each of these specific mechanisms. However, our experiments do not provide any evidence that warming of the tropical upper troposphere is sufficient for the differences in the jet response. In all of the experiments we have performed, there is stronger warming in the tropical upper troposphere than in any other region in the atmosphere (Figs. 2a,b and 1f; see also supplemental Fig. 1). This warming of the tropical upper troposphere is more pronounced in the JG17 configuration as compared to TLS19, even as the jet does not shift poleward in the JG17 configuration. More generally, configurations with a stronger tropical upper-tropospheric warming actually simulate a *weaker* poleward jet shift (Fig. 4b). Hence, we conclude that

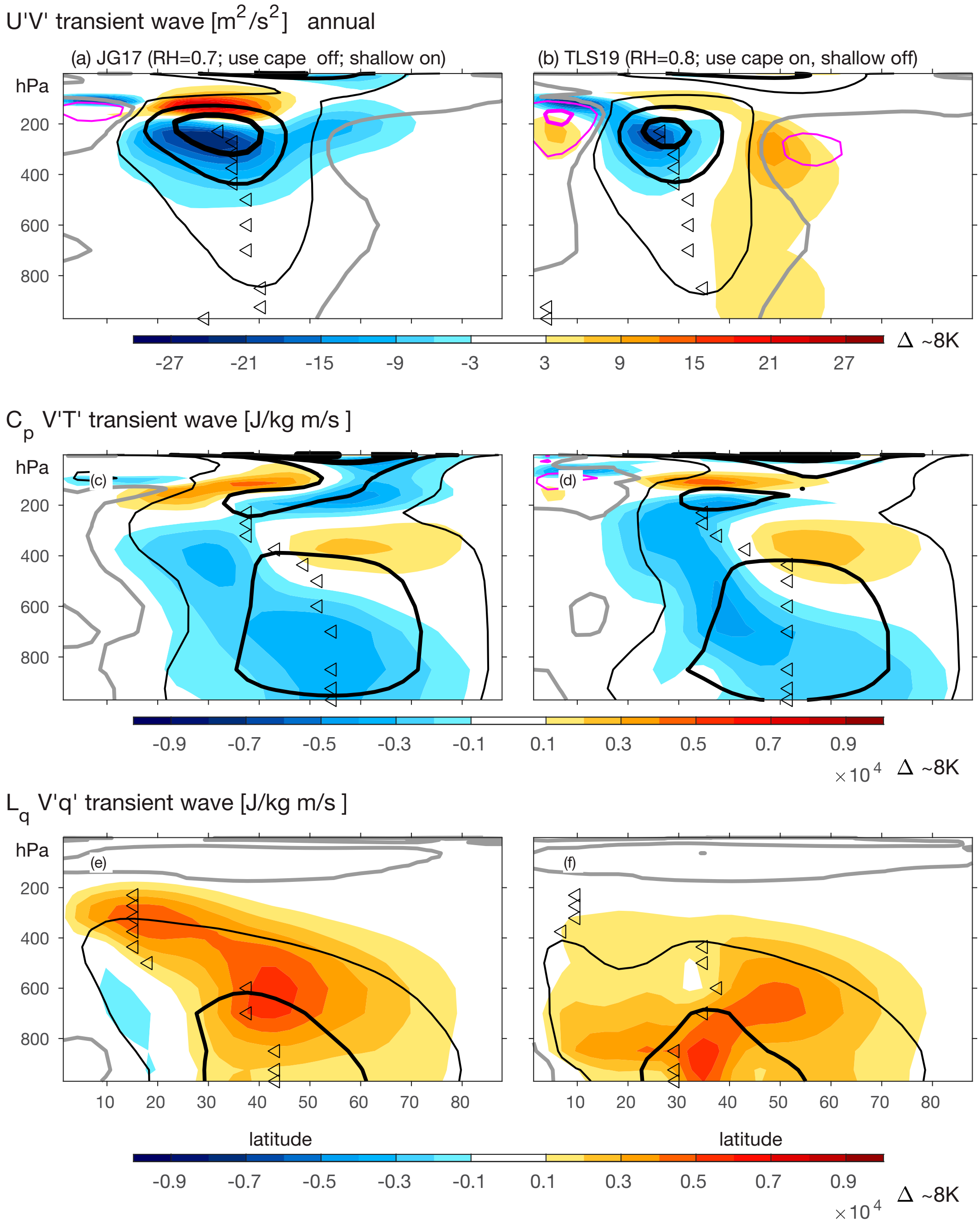

FIG. 5. Difference in latitude vs pressure (a),(b) $\overline{u'v'}$, (c),(d) $C_p\overline{v'T'}$, and (e),(f) $L_q\overline{v'q'}$ eddy fluxes between an ~8 K warming integration and a 1xCO$_2$ integration (shaded contours), and the climatological profile in the 1xCO$_2$ run (gray, black, and magenta lines) for the different aquaplanet configurations. Triangles denote the maximum in the present day simulation for each configuration and panel. (top) The contours for the black (positive) and magenta (negative) lines are at ±6, ±24, and ±48 m^2 s^{-2}, and the zero line is gray. (middle), (bottom) The contours for the black and magenta lines are at ±2000, ±8000, and ±16000 J kg^{-1} m s^{-1}, and the zero line is gray.

warming of the *tropical* upper troposphere alone (and by extension any of the subsequent distinct mechanisms that accompany it) is not of first-order importance for explaining the difference in jet shift across our experiments.

Enhanced tropical upper-tropospheric warming leads to a stabilization of the troposphere that is most pronounced in the deep tropics, but extends into the subtropics and midlatitudes. Previous work has argued that this stabilization of the subtropics relative to the midlatitudes could help to reduce eddy generation on the equatorward side of the jet, leading to a net poleward shift of the jet (Frierson 2008; Shaw 2019). Figures 2c and 2d show the changes in buoyancy frequency for JG17 and TLS19; in both there is a stabilization of the subtropical troposphere. This stabilization is more pronounced in the JG17 configuration, even as its jet does not shift poleward. More generally, configurations with a stronger subtropical stabilization actually simulate a *weaker* poleward jet shift (Fig. 4c), and hence this stabilization of the subtropics is not of first-order importance for explaining the diversity of jet shifts in our experiments.

Polar stratospheric cooling in response to increased GHG can also contribute to the poleward shift (Held 1993; Sigmond et al. 2004; Wu et al. 2012; Ceppi and Shepherd 2019), and we now consider whether this process is important in explaining the diversity in jet shifts. The polar stratosphere cools in response to increased GHG in all configurations (Figs. 2a,b); however, this cooling is more pronounced in the JG17 configuration and weaker in the TLS19 configuration. Overall, configurations with a more pronounced polar stratospheric cooling have a weaker poleward jet shift (Fig. 4d), opposite to naive expectations, and hence the stratospheric response is not of first-order importance for explaining the jet shift. This is not to deny that polar stratospheric variability can drive jet shifts on time scales ranging from the subseasonal to centennial (Garfinkel et al. 2013, 2023), but rather that this is not important for explaining the diversity of our model's circulation response to global warming.

A rising of the tropopause has been linked to a poleward jet shift (Lorenz and DeWeaver 2007). Following the World Meteorological Organization's (1957) definition, the tropopause height is estimated from temperature data as the lowest (in altitude) pressure level at which the lapse rate decreases to 2 K km^{-1}. The black and red pluses on Figs. 2a and 2b indicate the tropopause in each configuration, and the tropopause does indeed rise in our experiments, consistent with theoretical expectations (Held 1993; Vallis et al. 2015). This rising of the tropopause is evident for all configurations, however, and is of similar magnitude (Figs. 2c,d). Across all configurations, there is no relationship between the magnitude of the jet shift and the rising of the tropopause (Fig. 4e). Hence the rising of the tropopause is also not of first-order importance for explaining the differences in the jet shift.

Polar surface warming associated with Arctic amplification can help mitigate the poleward shift, and in isolation would induce an equatorward shift (Shaw et al. 2016; Cohen et al. 2020). We now consider whether this process could help account for the diversity in jet shifts. Arctic amplification is present in all configurations (Figs. 2a,b and 1e) despite the lack of sea ice, temperature-dependent albedo, or clouds in our model: Arctic amplification, at least in our model, is primarily associated with atmospheric moisture transport from the midlatitudes and tropics into the Arctic (Alexeev et al. 2005; Zhang et al. 2013). We find this to be stronger in the TLS19 configuration than JG17 (see the fluxes in the subpolar lower troposphere in Figs. 5e,f). Thus, Arctic amplification is strongest in the TLS19 configuration (green lines in Fig. 1e) and would, in isolation, lead to a weaker poleward shift, however TLS19 has a stronger poleward shift. A similar result is found when considering the other configurations: stronger polar amplification is found in configurations with a stronger jet shift, opposite to naive expectations (Fig. 4f). Hence Arctic amplification cannot be of first-order importance for causing the jet shift in any configuration.

Overall, we conclude that none of the above mechanisms related to the zonal-mean temperature response are of importance for the difference in jet shift across our configurations; this suggests that they are not of leading-order importance for driving the jet shift in TLS19, as they fail to predict a qualitatively different jet shift for this integration compared to JG17. These less relevant mechanisms include tropical upper-tropospheric warming, stabilization of the subtropics, polar stratospheric cooling, rising of the tropopause, and Arctic amplification.

b. *Is the jet shift determined by synoptic eddy processes: Feedback strength? Phase speeds? Length scale?*

Previous studies have posited that the jet shift is larger for integrations in which synoptic eddy feedback is stronger. Such a relationship was found to explain the magnitude of the response to polar stratospheric perturbations in the modeling study of Garfinkel et al. (2013), in which other mechanisms were not successful. This possibility is considered in Fig. 4g, which contrasts the jet shift to the *e*-folding time scale of the annular mode index. Following Garfinkel et al. (2013) or Baldwin and Thompson (2009), the annular mode index is the first principal component of 850-hPa zonally averaged daily zonal wind from 20° to the pole, weighted by $\cos^{1/2}$ of latitude, and its decorrelation time scale tracks the strength of eddy feedback (Lorenz and Hartmann 2001; Simpson et al. 2013). The relationship is weak. If anything, configurations with a more persistent first principal component actually simulate a weaker jet shift. Hence the difference in the poleward shift across the configurations is not associated with synoptic eddy feedback.

An additional proposed mechanism is that a strengthening of the subtropical jet (and more generally, of winds in the upper troposphere) leads to a shift toward higher-phase-speed eddies (Chen et al. 2008; Lu et al. 2008) and/or to a reduction of the meridional gradient of the absolute vorticity on the flanks of the jet (Kidston and Vallis 2012; Lorenz 2014), both of which may be expected to lead to more equatorward wave propagation and a poleward jet shift. First, we note that the subtropical jet strengthens in all experiments in this paper (Figs. 3a,b), even JG17 with an equatorward jet shift.

We diagnose this effect by computing the latitude–phase speed cospectrum of upper-tropospheric eddy momentum flux to characterize the meridional propagation of baroclinic eddies (Randel and Held 1991; Chen and Held 2007; Chen et al. 2008). The eddy momentum fluxes are first decomposed as a function of zonal wavenumber and frequency. Next, the cospectrum is transformed as a function of zonal wavenumber and angular phase speed. Finally, the momentum flux spectrum at each latitude is summed over wavenumber, resulting in a spectral density as a function of latitude and angular phase speed (Fig. 6).

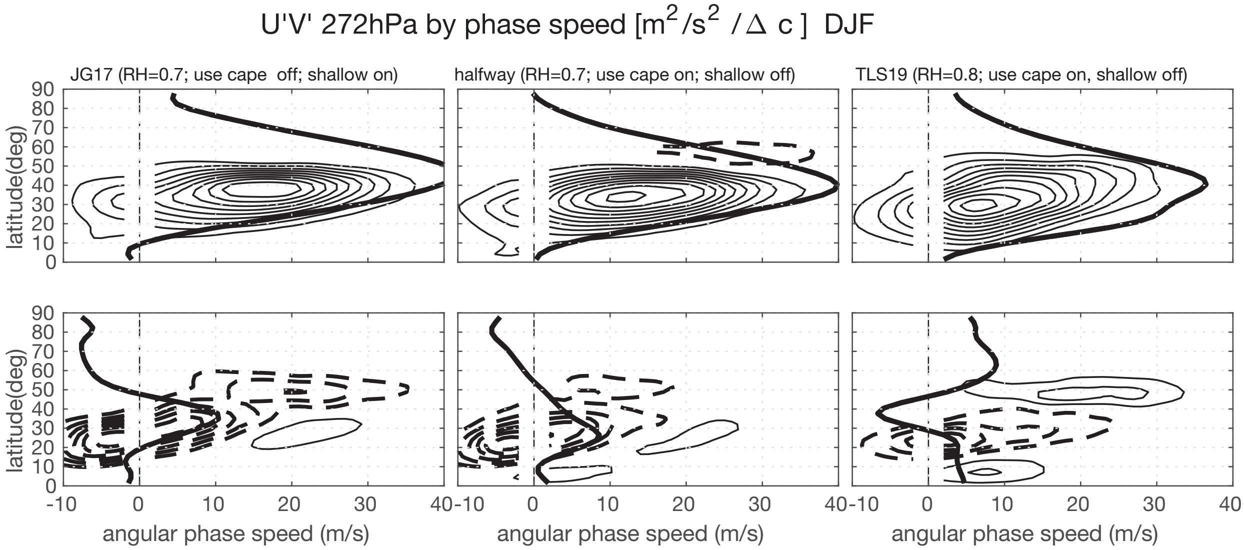

FIG. 6. Eddy momentum flux at 272 hPa decomposed by phase speed for the two aquaplanet configurations and one of the halfway configurations in (top) $1xCO_2$ run and (bottom) difference between a $1xCO_2$ integration and an ~8 K warming integration. Black lines indicate the (top) climatological jet in the $1xCO_2$ run (bottom) difference in jet response, with both divided by cosine of latitude.

In all configurations, as the upper-tropospheric jet strengthens, there is a sharper reduction in slow-phase-speed eddies than of faster-phase-speed eddies. This shift toward faster phase speeds does not, however, lead to a poleward jet shift in all configurations. Rather, for JG17, there is a dipole with enhanced eddy momentum flux near a phase speed of 20 m s^{-1} at 30°N, and reduced eddy momentum flux farther poleward, leading to an equatorward shift. In the TLS19 configuration, on the other hand, there is a poleward shift of the eddy momentum flux for phase speeds exceeding 10 m s^{-1}. Hence, both experiments with and without a poleward jet shift feature a shift toward faster phase speeds and a faster subtropical jet. The magnitude of the area-weighted shift of momentum flux toward faster phase speeds, averaged over all latitudes, is shown on the ordinate of Fig. 4i. Across all configurations, a stronger shift toward faster phase speeds is actually associated with a weaker jet shift, opposite to naive expectations. Hence, the shift toward faster phase speeds is not of first-order importance for explaining the diversity of jet shifts in the different configurations.

Finally, previous works have argued that increased GHG leads to a shift of eddy length scales toward longer waves (Kidston et al. 2010; Barnes and Hartmann 2011; Rivière 2011; Kidston et al. 2011; Chemke and Ming 2020). As longer scales are more likely to break anticyclonically and/or on the equatorward flank of the jet (Rivière 2011; Kidston et al. 2011), this could then lead to a poleward shift. Figure 7 decomposes the changes in eddy heat flux and eddy momentum flux into its wavenumber components. For both momentum and heat fluxes, there is indeed a shift toward lower wavenumbers: eddy fluxes decrease for wavenumbers 6–8 and increase for wavenumbers 1–3. This change, however, is evident for all experiments, including those with and without a poleward shift. If anything, it is stronger in JG17 despite the lack of a poleward jet shift. Across all configurations, there is little relationship between the magnitude of the shift toward longer wavelengths and the magnitude of the jet shift (Fig. 4h). Hence the increase in eddy length scale cannot be a leading cause of the differences in jet shift among the configurations.

c. *Insights from an energetic perspective*

Shaw (2019) also considers a number of mechanisms that focus on the energetics of the midlatitude circulation. Two of the mechanisms start with the assumption that the poleward flux of moist static energy is effectively constant in time. Changes in the poleward flux of storm track moist static energy (MSE) by zonal eddies ($L_q\overline{v'q'} + g\overline{v'Z'} + C_p\overline{v'T'}$ where x' denotes a deviation from the zonal average and $\overline{x}$ indicates the zonal mean) are shown in Figs. 3e and 3f [calculated as in Eq. (3) of Donohoe et al. (2020)]. In all configurations the MSE flux strengthens in the midtroposphere in midlatitudes. Changes elsewhere, however, differ across the configurations: only in the TLS19 configuration is there a north–south dipole in the MSE flux in the midtroposphere. Further, the lower-tropospheric flux differs qualitatively depending on the use of a shallow convection scheme. The increased lower-tropospheric MSE flux when shallow convection is off is driven by $L_q\overline{v'q'}$ (Figs. 3e,f). This likely occurs because as specific humidity increases in both configurations (Figs. 2e,f), convective precipitation increases only in JG17 but not in TLS19 (Fig. 1j); hence, the resolved MSE flux must increase mainly in TLS19 to balance the increase in energy input and flux away energy (Fig. 1k).

These differences in moist static energy are mainly associated with differences in the latent energy flux rather than dry static energy. Figures 5c and 5d shows the changes in the sensible eddy heat flux ($C_p\overline{v'T'}$; the changes in $g\overline{v'Z'}$ are negligible); in all experiments the changes are essentially indistinguishable. Sensible eddy heat fluxes weaken in the lower troposphere (with the

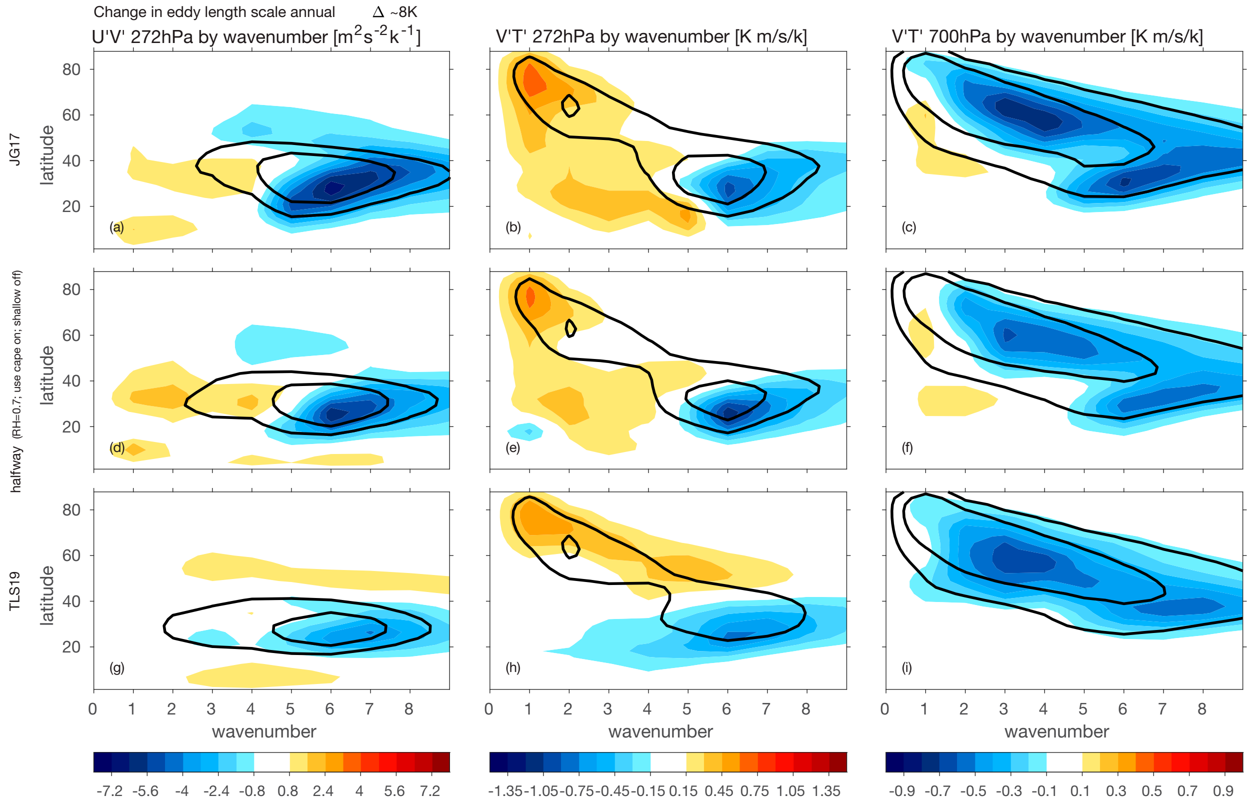

FIG. 7. Difference in eddy heat and momentum fluxes between a ∼8 K warming integration and a $1\mathrm{xCO_2}$ integration for the aquaplanet configurations decomposed by zonal wavenumber for (left) $\overline{u'v'}$ at 272 hPa, (center) $\overline{v'T'}$ at 272 hPa, and (right) $\overline{v'T'}$ at 700 hPa. Black contours indicate the climatological profile in the $1\mathrm{xCO_2}$ run, and are shown at 4 and 7.2 $\mathrm{m^2\,s^{-2}}\,k^{-1}$ for the left column, 0.5 and 0.9 $\mathrm{K\,m\,s^{-1}}\,k^{-1}$ for the center column, and 0.5 and 1.575 $\mathrm{K\,m\,s^{-1}}\,k^{-1}$ for the right column.

weakening stronger in JG17, even as the Arctic amplification is less pronounced than in TLS19), and shift poleward in the upper troposphere. These changes in the sensible eddy heat flux are overwhelmed in most regions by changes in the latent eddy energy fluxes (Figs. 5e,f; supplemental Fig. 6), which differ substantially across the experiments. Therefore, a mechanism which starts with the assumption that MSE flux is constant in response to increased GHG is not relevant to our model setup. The total eddy MSE poleward flux increases substantially in response to increased GHG in all of our configurations.

Indeed, previous work has found that the eddy flux of moist static energy can increase in response to GHG if the gradient in net energy input from the equator to the pole also increases (Hwang et al. 2011; Barpanda and Shaw 2017; Shaw et al. 2018; Shaw 2019). We next evaluate whether this mechanism can account for the changes in storm track intensity that are evident in Figs. 3e and 3f.

The pressure-weighted integral of the change in net energy input is shown in Fig. 8a. Energy input increases in the tropics and decreases in subpolar latitudes in all experiments. This is driven mainly by changes in outgoing longwave radiation (not shown). Such a change will be associated with an overall increase in the flux of moist static energy, assuming energy transport by oceans does not change, which is explicitly the case in our model. This flux can be driven both by eddy fluxes and zonal-mean fluxes, and indeed both respond to global warming: eddy transport increases at all latitudes (Fig. 8b), and the zonal-mean moist static energy flux ($\overline{v}\,\overline{\mathrm{mse}}$) increases outside of the tropics.

At nearly all latitudes, the moist static energy flux both from the zonal mean and from the eddies increases, to balance the increase in equator-to-pole gradient of the energy input. However, the relative role of eddy versus zonal-mean terms in balancing the increase in the equator-to-pole gradient of the energy input differs among the configurations. The net effect of this delicate balance is that the poleward shift (or lack thereof) in the near-surface jet is tightly coupled to the poleward shift in the latitude of the maximum in eddy MSE flux (Barpanda and Shaw 2017; correlation of 0.89, similar to Fig. 4a). This includes an equatorward shift in the latitude of the maximum in eddy MSE flux in JG17 because the increase in the eddy MSE flux on the equatorward flank of the climatological maximum near 45° is larger than that on the poleward flank (Fig. 8b). Nonetheless these changes do not readily account for the vertical structure evident in Fig. 3. Specifically, moist static energy fluxes increase in the subtropical lower troposphere, but decrease in the subtropical upper troposphere in TLS19, a

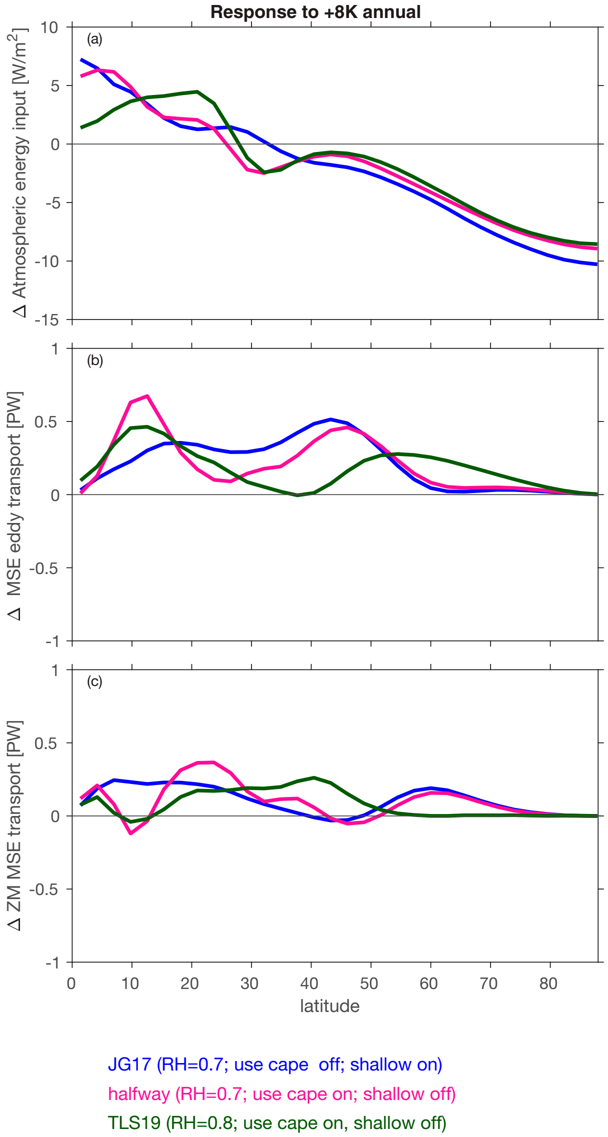

FIG. 8. Latitudinal structure of the difference between an ~8 K warming integration and a 1xCO_2 integration of the (a) energy input and (b),(c) energy transport by eddies and zonal-mean circulation for the different aquaplanet configurations.

feature not readily explainable by the energetic perspective. Overall, the energetic changes are consistent with the jet shift. Additional insight, however, can be gained by incorporating the momentum budget explicitly in the closure, as the momentum budget helps clarify the relative importance of different vertical levels for explaining the jet shift.

5. Insight into the jet shift by combined energetic and momentum balances

Thus far, our results have been chiefly destructive, ruling out many of the proposed mechanisms for the jet response. We attempt to be more constructive in this section. Specifically, our approach is to use the steady-state thermodynamic heat budget (introduced below) to connect the thermodynamic response to the dynamical response to increased GHGs. In particular, we link the diabatic heating and static stability responses to the time-mean and zonal-mean vertical velocity response, which in turn is linked to the Ferrel cell and latitude of surface westerlies.

a. *Thermodynamic starting points*

Our perturbations to the convection scheme have a direct impact on latent heat release both in the climatology and in response to increased GHG (Figs. 9a,b; supplemental Fig. 3). The climatological convective heating (black contours) in the subtropics differs in structure between the configurations: in JG17, convective heating is present throughout the subtropics, but in TLS19 there is a gap in convective heating between the tropics and midlatitudes. The response of convective heating to increased GHG (i.e., Δconvective heating) in the subtropics also differs between these configurations: there is a reduction in JG17, but no change in TLS19 (as convective heating cannot go negative). Further, the increase in diabatic heating poleward of the jet between 55° and 75° in the mid- and lower troposphere is more pronounced in TLS19 than in JG17. These changes in convective heating dominate the total diabatic heating associated with moist processes (Figs. 9c,d).

In contrast to the Δconvective heating, which differ strongly between JG17 and TLS19, the Δradiative heating and Δboundary layer heating are similar between JG17 and TLS19 (Figs. 9g,h). There is enhanced radiative cooling to space under increased GHG of roughly similar magnitude, consistent with the similar ΔT in all experiments. The sum of all diabatic terms is shown in Figs. 9i and 9j, and differences in Δdiabatic heating are evident in two key regions:

1) In the subtropics, the reduction in diabatic heating is more pronounced in the JG17 configuration as compared to TLS19. This is likely related to the fact that there is more convection to begin with in the subtropics in the JG17 and hence more to lose, and also to a stronger stabilization of the subtropics in JG17 with the shallow convection scheme turned on.
2) Poleward of the climatological jet from 55° to 75°, the increase in diabatic heating is more pronounced in TLS19 in the mid- and lower troposphere. That is, the tail that extends downward and poleward from the region of strongest response is stronger for TLS19 (see the box on Fig. 9). Note that large-scale precipitation changes are essentially identical in all configurations (Fig. 1k), and hence this difference in convective diabatic heating is not predetermined by the changes in the large-scale dynamics. Rather, it arises because of the convection parameterization which is more easily triggered at subpolar latitudes in a globally warmed climate if TLS19 settings are used (Fig. 1j). Similarly, large-scale latent and radiative heating actually decrease in the subpolar midtroposphere in response to warming (supplemental Fig. 3), and hence the convective scheme alone (and not the synoptic dynamics) is driving this increase in diabatic heating.

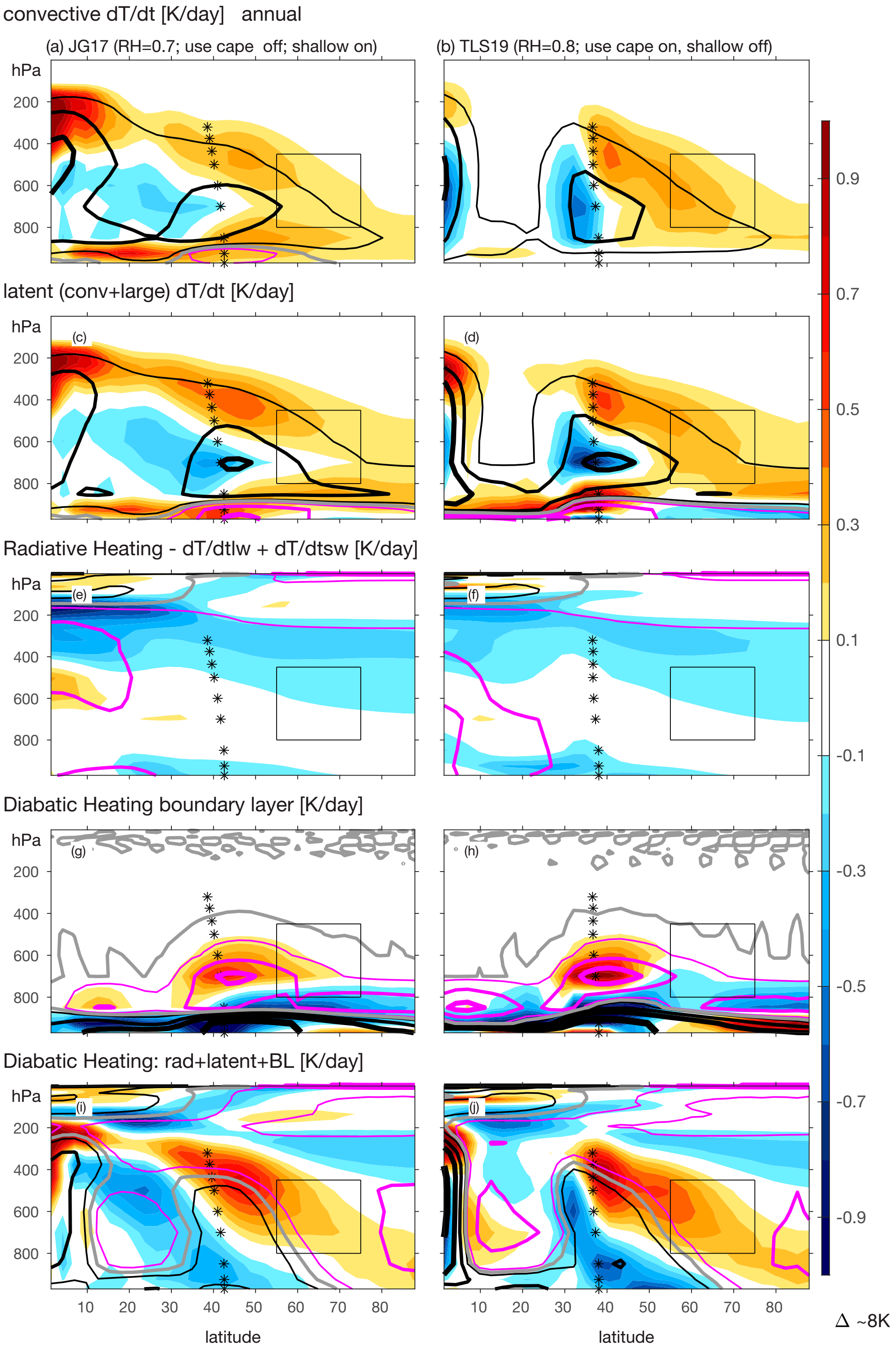

FIG. 9. Difference in latitude vs pressure diabatic heating rates between an ~8 K warming integration and a 1xCO$_2$ integration (shaded contours), and the climatological profile in the 1xCO$_2$ run (black and magenta lines), for the different aquaplanet configurations. (a),(b) Convective latent heat release; (c),(d) total latent heat release by convection and large-scale precipitation; (e),(f) radiative heating (both shortwave and longwave); (g),(h) boundary layer heating; (i),(j) sum of latent, radiative, and boundary layer heating. Asterisks denote the climatological jet latitude, and a rectangle encloses the region focused upon in section 5 and Figs. 4j–l. The contours for the black (positive) and magenta (negative) lines are at ±0.3, ±1.2 and ±2.4 K day^{-1}, and the zero line is gray.

These two differences are referred to as thermodynamic starting points in the rest of this paper.

In addition to these differences in Δdiabatic heating among the configurations, a third thermodynamic starting point is the static stability for each configuration (Figs. 2c,d). While there is a stabilization of the troposphere in all configurations, the stabilization is stronger in the JG17 configuration as the increased prevalence of convection leads to a climatological temperature profile closer to a moist adiabat. As described below, we find that of these three thermodynamic starting points, the second (diabatic heating poleward of the jet core) is apparently the most important for the differences in poleward shift, as it is most tightly linked with the poleward shift of the upwelling region of the Ferrel cell.

b. *Blending the heat, mass, and momentum budgets*

Even though the eddy-driven jet latitude is ultimately determined by eddy momentum fluxes, it is also linked with the eddy heat flux and diabatic heating. Lachmy and Kaspi (2020) and Lachmy (2022) found this relationship to be relevant for jet latitude both in reanalysis data and CMIP output. We first summarize their results before applying them to our simulations. They combine balances of mass, momentum, and energy, to link the jet latitude to the diabatic heating. The conservation of mass and momentum ties upwelling and downwelling in the Ferrel cell to the jet location: the maximum in surface meridional winds is collocated with the maximum surface westerlies, thus allowing for the Coriolis torque on the meridional flow to be balanced by surface drag. Upwelling on the poleward half of the Ferrel cell (poleward of the surface westerly maximum) leads to adiabatic cooling, which must be balanced by eddy heat flux convergence and/or diabatic heating. Conversely, adiabatic warming on the equatorward half of the Ferrel cell must be balanced by eddy heat flux divergence and/or diabatic cooling. Here, we investigate how changes in the convection scheme influence the role of diabatic heating in balancing the adiabatic tendencies of the Ferrel cell.

Our diagnostic tool is the temperature budget. Following Eq. (1) of Lachmy and Kaspi (2020) and Lachmy (2022) and using their notation, the budget can be expressed as

$$\frac{\partial\overline{T}}{\partial t} = -\frac{\overline{v}}{a}\frac{\partial\overline{T}}{\partial\phi} - \overline{\omega}\left(\frac{\partial\overline{T}}{\partial p} - \kappa\frac{\overline{T}}{p}\right) - \frac{1}{a\cos\phi}\frac{\partial[\cos\phi(\overline{v'T'})]}{\partial\phi} - \left[\frac{\partial(\overline{\omega'T'})}{\partial p} - \kappa\frac{(\overline{\omega'T'})}{p}\right] + \frac{\overline{J}}{C_p}, \qquad (1)$$

where $\overline{x}$ refers to the zonal mean and x' to the perturbation from the zonal mean. For a statistically steady state, the temperature is constant in time ($\partial\overline{T}/\partial t = 0$), so the right-hand side of Eq. (1) must equal zero. This implies that the $\overline{\omega}(\partial\overline{T}/\partial p - \kappa\overline{T}/p)$ term in Eq. (1), which represents adiabatic heating due to zonal-mean vertical motion, must balance the other terms on the right-hand side. That is,

$$\overline{\omega}\left(\frac{\partial\overline{T}}{\partial p} - \kappa\frac{\overline{T}}{p}\right) = -\frac{\overline{v}}{a}\frac{\partial\overline{T}}{\partial\phi} - \frac{1}{a\cos\phi}\frac{\partial[\cos\phi(\overline{v'T'})]}{\partial\phi} - \left[\frac{\partial(\overline{\omega'T'})}{\partial p} - \kappa\frac{(\overline{\omega'T'})}{p}\right] + \frac{\overline{J}}{C_p}. \qquad (2)$$

The right-hand side of Eq. (2) is dominated by the eddy heat flux convergence and diabatic heating, while $(\overline{v}/a)(\partial\overline{T}/\partial\phi)$ is small (see supplemental Fig. 4). In the remainder of this section, the stability term $(\partial\overline{T}/\partial p - \kappa\overline{T}/p)$ will be denoted by S for simplicity.

We calculate each term in this budget for each integration, and first validate that the budget indeed closes, both in the climatology and in the response to increased CO$_2$, in Fig. 10. Figures 10c and 10d show the sum of all the eddy terms, while Figs. 10e and 10f shows the sum of the right-hand side of Eq. (2), which opposes $\overline{\omega}S$ (Figs. 10g,h). The residual of Eq. (2) is shown to be generally negligible in Figs. 10i and 10j, with truncation and round-off errors relatively small. Each of the individual terms on the right-hand side of Eq. (2) is shown in Fig. S4.

The link between the Ferrel cell and the near-surface maximum westerlies is verified in Figs. 11a and 11b. The magenta contour in midlatitudes in Figs. 11a and 11b (i.e., the climatological Ferrel cell) is collocated with the maximum westerlies in the lower troposphere and near the surface. Figures 11a and 11b also show that the Ferrel cell response to increased CO$_2$ differs among the integrations, with a weakening in JG17 and a poleward shift in TLS19. Lower-tropospheric meridional winds also respond differently between JG17 versus TLS19, with a poleward shift of the maximum southerlies for TLS19 only (not shown). This difference between JG17 and TLS19 reflects consistency with the difference in the jet shifts, as the jet shift is ultimately regulated by the Coriolis torque acting on the surface southerlies of the Ferrel cell.

c. *Applying the heat budget to interpret the difference in jet shift*

The balance expressed in Eq. (2) holds in both the present-day integration and in response to enhanced CO$_2$. Hence, we can use this balance to interpret the difference in jet shift between JG17 and TLS19. This framework cannot assess causality; nevertheless, it can clarify which of the thermodynamic starting points listed in section 5a is most important for balancing the Ferrel cell response, and subsequently the near-surface westerlies response, that differ among the configurations.

The changes on the right-hand side of Eq. (2), denoted $\Delta\mathrm{RHS}_{\mathrm{eq2}}$, are noticeably different between JG17 and TLS19 (Figs. 10e,f) both in the subtropics and poleward of the jet core. What are the implications of this difference in $\Delta\mathrm{RHS}_{\mathrm{eq2}}$ (or equivalently, $\Delta\overline{\omega}S$) for the Ferrel cell mass circulation? To answer this question, we need to separately consider changes in S (similar to Figs. 2c,d) and changes in ω (Figs. 11c,d). Specifically, the changes in $\Delta\mathrm{RHS}_{\mathrm{eq2}} = \Delta(\overline{\omega}S) = \overline{\omega_{+8\mathrm{K}}}S_{+8\mathrm{K}} - \overline{\omega_{\mathrm{PD}}}S_{\mathrm{PD}}$ can be approximated as $\Delta(\overline{\omega}S) \approx (\overline{\omega_{\mathrm{PD}}} + \Delta\overline{\omega})(S_{\mathrm{PD}} + \Delta S) - \overline{\omega_{\mathrm{PD}}}S_{\mathrm{PD}}$, where the subscript PD refers to present day. (The approximation arises because we now are neglecting time variability in $\overline{\omega}$ and S, and instead consider only the product of their time means.) After

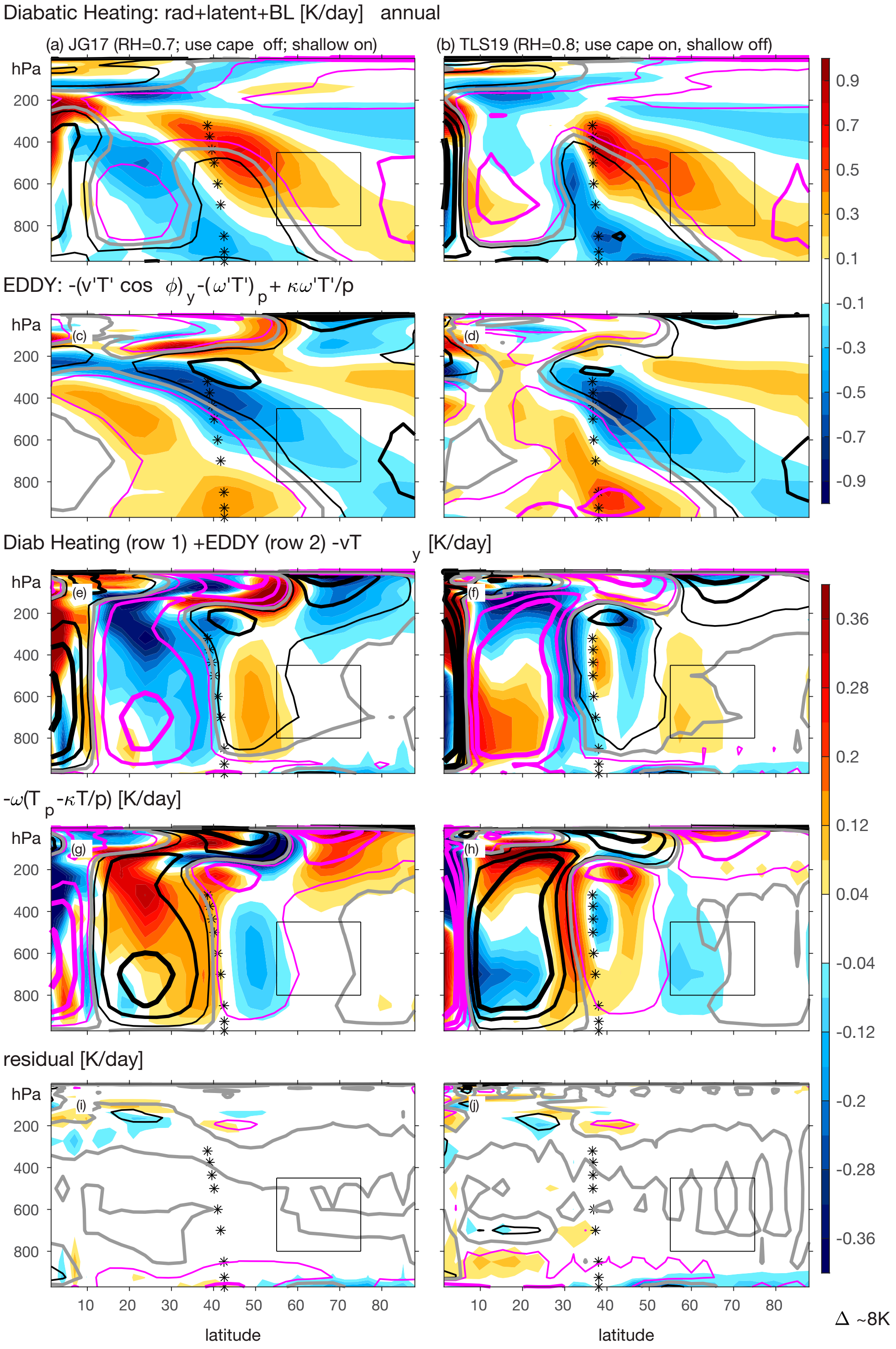

FIG. 10. Difference in latitude vs pressure of terms in the thermodynamic budget [Eq. (2)] between an ~8 K warming integration and a 1xCO_2 integration (shaded contours), and the climatological profile in the 1xCO_2 run (gray, black, and magenta lines) for the different aquaplanet configurations: (a),(b) diabatic heating (repeated from Fig. 9); (c),(d) eddy terms; (e),(f) sum of the diabatic heating term, eddy term, and $(\overline{v}/a)(\partial \overline{T}/\partial \phi)$; (g),(h) Ferrel cell term $\overline{\omega}(\partial \overline{T}/\partial p - \kappa \overline{T}/p)$; and (i),(j) residual of Eq. (2). Asterisks denote the climatological jet latitude, and a rectangle encloses the region focused upon in section 5 and Figs. 4j–l. The contours for the black (positive) and magenta (negative) lines for (a)–(d) are at ± 0.3, ±1.2, and ±2.4 K day^{-1}, and the zero line is gray. For (e)–(j), the contours for the black and magenta lines are at ±0.08, ±0.32, and ±0.64 K day^{-1}, and the zero line is gray.

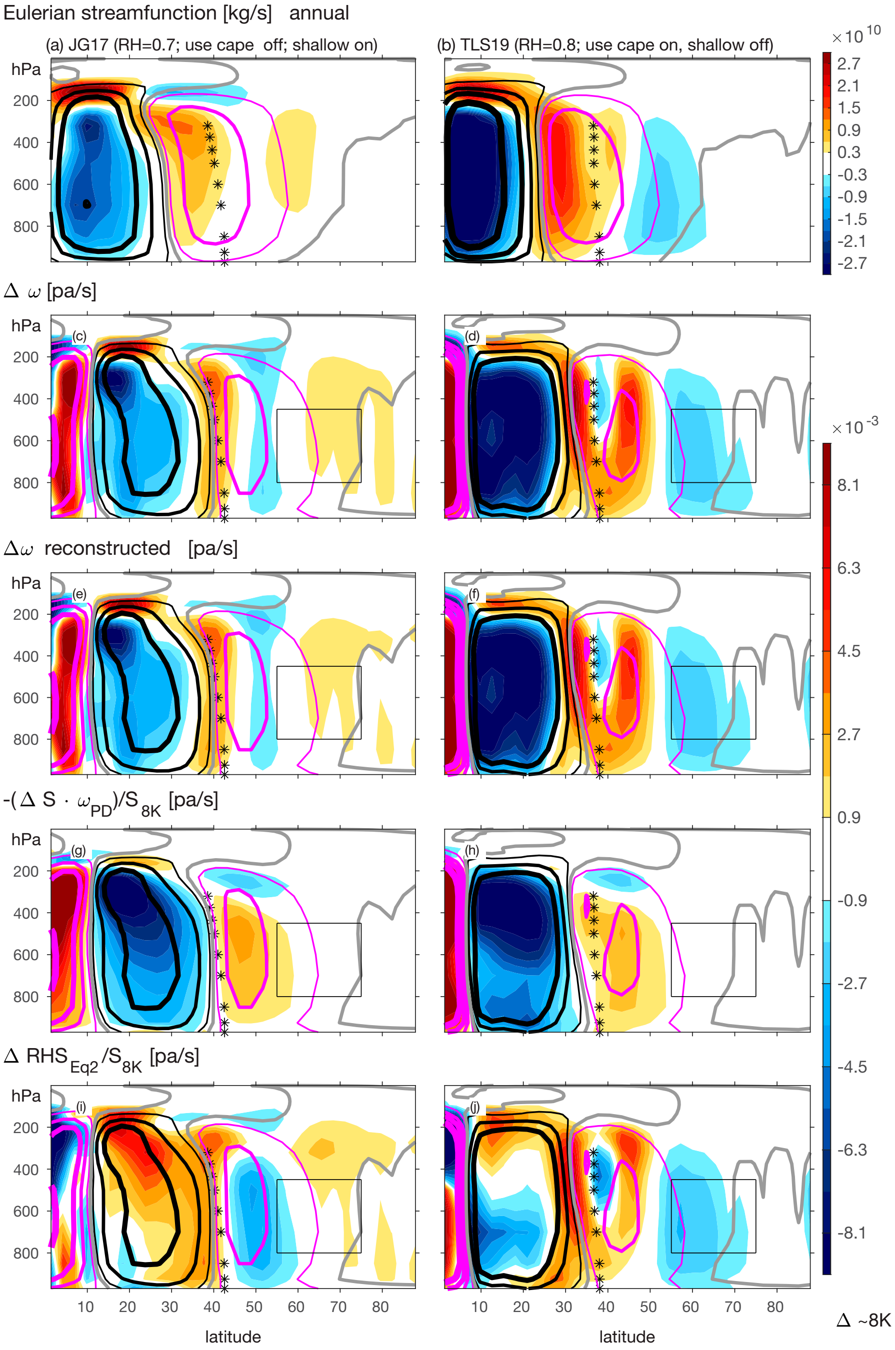

FIG. 11. Difference in latitude vs pressure of terms related to the Eulerian streamfunction between an ~8 K warming integration and a 1xCO$_2$ integration (shaded contours), and the climatological profile in the 1xCO$_2$ run (gray, black, and magenta lines), for the different aquaplanet configurations: (a),(b) Eulerian mass streamfunction [computed by integrating $\overline{v} = [g/(2\pi a \cos\phi)](\partial\Psi/\partial p)$; see Eq. (3) of Lachmy and Kaspi (2020)]; (c),(d) ω as simulated in the model; (e),(f) reconstructed ω using Eq. (3); (g),(h) second term on the right-hand side of Eq. (3) ($-\Delta S \omega_{\mathrm{PD}}/S_{8\mathrm{K}}$); and (i),(j) first term on the right-hand side of Eq. (3) ($\Delta\mathrm{RHS}_{\mathrm{eq2}}/S_{8\mathrm{K}}$). Asterisks denote the climatological jet latitude, and a rectangle encloses the region focused upon in section 5 and Figs. 4j–l. The black and magenta lines for (c) and (d) are repeated for subsequent rows. The contours for the black (positive) and magenta (negative) lines in (a) and (b) are shown at $\pm 6 \times 10^9$, $\pm 2.4 \times 10^{10}$, $\pm 4.8 \times 10^{10}$, $\pm 9.6 \times 10^{10}$ kg s^{-1}, and for (c)–(j) at ± 0.0018, ± 0.0072, and ± 0.0144 Pa s^{-1}.

some algebra, we find that $\Delta(\overline{\varpi}S) \approx \Delta\overline{\varpi}S_{\mathrm{PD}} + \Delta S\overline{\varpi_{\mathrm{PD}}} + \Delta S\Delta\overline{\varpi}$, which can be rearranged to

$$\Delta\overline{\varpi} \approx \frac{\Delta(\mathrm{RHS}_{\mathrm{eq2}}) - \Delta S\overline{\varpi_{\mathrm{PD}}}}{S_{+8\mathrm{K}}}. \qquad (3)$$

Equation (3) links the change in the Ferrel cell mass circulation to the changes in the sum of the diabatic heating and dry eddy heat fluxes, and also the static stability. Specifically, if the $\Delta\mathrm{RHS}_{\mathrm{eq2}}$ [and hence $\Delta(\overline{\varpi}S)$] and ΔS are known, then $\Delta\omega$ and hence the Ferrel cell mass circulation can be deduced. Note that the reconstructed change in ω from Eq. (3) is essentially equal to the actual change in ω (Figs. 11c,d vs Figs. 11e,f; Fig. S5), and hence the approximations leading up to Eq. (3) are validated.

We now analyze each of the terms in Eq. (3), to highlight how changes in the $\mathrm{RHS}_{\mathrm{eq2}}$ versus in the static stability balance the total change in ω (Figs. 11g–j). In the subtropics, downwelling weakens in both configurations, but the total adiabatic heating by the downwelling nevertheless increases (Figs. 10g,h), especially for JG17. This is due to the static stability response: the change induced by the $\Delta S\overline{\varpi_{\mathrm{PD}}}$ term [Figs. 11g,h; the second term on the numerator of Eq. (3)] overwhelms the $\Delta\mathrm{RHS}_{\mathrm{eq2}}$ term (Figs. 11i,j). Near the climatological jet latitude, both terms are important. In contrast, well poleward of the jet core (>55°), the $\Delta\mathrm{RHS}_{\mathrm{eq2}}$ term is more important than $\Delta S\overline{\varpi_{\mathrm{PD}}}$, suggesting that stabilization of the midlatitudes under climate change cannot explain the poleward shift of the Ferrel cell (and jet) for TLS19 versus the equatorward shift in JG17 (in agreement with section 4a).

Of particular importance for the Ferrel cell changes are the changes in ω between 50° and 65° (Figs. 11e,f). Increased GHG leads to anomalous rising motion at 50° and subsidence at 65° in JG17, but the reverse in TLS19. These changes in ω reflect a poleward shift of the Ferrel cell in TLS19 only (Figs. 11a,b), consistent with the fact that surface westerlies shift poleward only in TLS19 (this last point is confirmed by solving the Kuo-Eliassen equations or examining the near-surface southerlies of the Ferrel cell; not shown). At these latitudes, the total $\Delta\omega$ is dominated by $\Delta\mathrm{RHS}_{\mathrm{eq2}}$, and $\Delta\mathrm{RHS}_{\mathrm{eq2}}$ differs qualitatively between JG17 and TLS19. The subpolar $\Delta\mathrm{RHS}_{\mathrm{eq2}}$ is dominated by Δdiabatic heating (Figs. 10a,b): the increase in diabatic heating between 55° and 75° is stronger in TLS19 than in JG17 (see the box on Fig. 11). The relatively stronger increase in diabatic heating in TLS19 is, in turn, dominated by stronger convective heating in this region (Figs. 9a–d). Hence, the stronger increase in midlatitude diabatic heating well poleward of the jet in TLS19 versus in JG17 is balanced by changes in the Ferrel cell that imply a poleward shift in TLS19 only of the surface westerlies.

This relationship is summarized in Fig. 4j, which contrasts the magnitude of the strengthening in midlatitude diabatic heating poleward of the jet (ordinate) with the jet shift (abscissa); across all configurations, a stronger increase in diabatic heating is associated with a stronger jet shift, consistent with the relationship in TLS19 and JG17. The relationship is entirely due to convective diabatic heating (Fig. 4k), while the other diabatic heating terms provide a weak negative feedback (Fig. 4l).

In summary, the steady-state thermodynamic budget directly connects the stronger increase in convective heating well poleward of the jet in TLS19 as compared to JG17 (Figs. 9c,d), to the poleward shift in TLS19. The changes in the subtropics, on the other hand, are comparatively unimportant.

6. Discussion and summary

Climate models project a poleward shift of the zonal-mean midlatitude jet and storm track in response to increased greenhouse gas (GHG) concentrations. The poleward shift has important implications for hydroclimate and weather extremes in heavily populated regions. The specific mechanism(s) causing this shift are poorly constrained: several dozen different mechanisms have been proposed, but there is little understanding of which are important (Shaw 2019). Further, the magnitude of the shift differs across models (O'Gorman 2010; Kidston and Gerber 2010; Gerber and Son 2014; Simpson and Polvani 2016; Curtis et al. 2020; Garfinkel et al. 2020a). This uncertainty in the magnitude dominates the overall uncertainty in future hydroclimate changes (Elbaum et al. 2022).

Climate models are not run at resolutions that explicitly resolve convection. Rather, convection is parameterized in order to represent known physical processes that lead to precipitation. These convection parameterizations are still undergoing updates to better match observations, and the underlying physical assumptions differ across models (Rio et al. 2019; Bartana et al. 2022; Lin et al. 2022). The net effect is that across different comprehensive CMIP5/6 models, the relative fraction of convective versus large-scale tropical precipitation differs from an even split to essentially all convective (Fig. 1 of Chen et al. 2021). Our goal was to change the settings of the convection scheme of our model so as to cover, if not slightly exaggerate, this range.

In our model, the relative ratio of large-scale to convective tropical precipitation is mainly sensitive to two parameter settings: the relative humidity profile toward which the atmosphere relaxes to remove convective instability (RHrelax), and whether we use a shallow convection scheme to redistribute moisture upward above the boundary layer. When these two settings are chosen to reduce tropical convection in the model, instead allowing for more large-scale precipitation [following Tan et al. (2019, hereafter TLS19)], a robust poleward shift is evident in response to global warming. When the convection scheme dominates the overall tropical latent heating [following Jucker and Gerber (2017, hereafter JG17)], however, a weak equatorward shift is found instead.

More than 20 distinct mechanisms have been proposed to explain changes in the jet and storm track in response to increased GHG (Shaw 2019). Most of them, however, are unable to explain the difference in response to increased GHG between the TLS19 configuration and the JG17 configuration. The "unhelpful" mechanisms include nearly all of the thermodynamic starting points and pathways thought to explain the poleward shift reviewed by Shaw (2019): tropical upper-tropospheric warming, Arctic amplification, rising of the tropopause, stratospheric cooling, a shift toward longer eddy wavelength, and a shift toward faster eddy phase speeds. This suggests that these mechanisms are not of first-order importance for the jet shift: if they were, then they should be able to account for the difference in jet shift between TLS19 and JG17, as they are just as active in both. This supports other recent studies that found tropical upper-tropospheric warming to be relatively unimportant (Shaw and Tan 2018; Shaw 2019; Tan and Shaw 2020). The annular mode time scale and climatological jet position are also similar in all configurations, and thus cannot explain the difference in response. As clouds are not present in either model configuration, cloud radiative effects cannot explain the spread in response by construction. While we cannot exclude these effects as being important in more realistic modeling configurations, these effects cannot be the only important factor explaining the poleward shift of the storm track and jet.

So, what does explain the poleward shift in response to increased CO_2? There are three thermodynamic starting points that differ between the JG17 and TLS19 configurations: the stabilization of the tropical and subtropical troposphere is stronger in JG17 (Figs. 2c,d), the increase in latent heating in response to increased GHG between 55° and 75° is stronger in TLS19 (Fig. 9), and the decrease in latent heating in response to increased GHG between 15° and 30° is stronger in JG17 (Fig. 9). All three of these responses are related directly to the convection parameterization and are not trivially a consequence of the jet shifts (e.g., if the jet response drove the subpolar latent heat increase, then we would expect large-scale latent heating to also increase, however there is no comparable increase in subpolar large-scale latent heating; see supplemental Fig. S3). The relative importance of these three thermodynamic starting points for balancing the jet shift can be elucidated by the steady-state thermodynamic budget. Specifically, the budget identifies the relatively stronger increase in convective heating well-poleward of the jet in response to increased GHG evident in TLS19 as compared to JG17 (Figs. 9c,d), as a crucial difference associated with the poleward shift in TLS19.

The increase in diabatic heating on the poleward flank of the jet balances the strengthening of the upwelling branch of the Ferrel cell at these subpolar latitudes, and thus balances the poleward shift of the entire Ferrel cell (Figs. 11a,b). As the latitude of the maximum streamfunction of the Ferrel cell must collocate with the latitude of the surface westerlies (drag on the surface westerlies is balanced by the Coriolis torque associated with the surface southerlies of the Ferrel cell), this poleward shift of the Ferrel cell must be accompanied by a poleward jet shift in TLS19. In contrast, in JG17, the weak changes in subpolar diabatic heating are fully mitigated by changes in temperature fluxes by dry eddies. We acknowledge the caveat that this budget argument does not demonstrate causality, and additional work is needed to demonstrate a causal connection between the subpolar diabatic heating and the jet shift. Specifically, while the right-hand side of Eq. (2) does indeed constrain the Ferrel cell latitude, it is not obvious from first principles that the eddy sensible heat flux [which constitutes part of the right-hand side of Eq. (2)] would be less important.

While we find that the response of diabatic heating poleward of the jet core is part of the jet response, this does not mean that more moisture generally leads to a strong jet response. The poleward flux of moisture increases in all simulations under increased CO_2 (Figs. 5e,f; supplemental Fig. 6). Figure 12 shows the correlation of the jet response with the specific humidity response across all 10 configurations as a function of latitude and pressure; an essentially similar result is found if we replace specific humidity response with the moist static energy response. Throughout the entire tropics, a stronger increase in moisture is associated with a weaker jet shift. Similarly, a stronger increase in moisture poleward of the jet is also associated with a weaker jet shift. Positive correlations (i.e., more moisture leads to a stronger shift) are found only in a narrow region equatorward of the climatological jet between 30° and 40° in the boundary layer. Future work should consider the role of moisture in this region specifically for the subsequent diabatic heating response farther poleward. Further, we note that Tan and Shaw (2020) also found a stronger moisture gradient in midlatitudes is associated with a poleward shift, consistent with our results. Our results also support those of Dwyer and O'Gorman (2017), who found that changes in the dry eddy heat fluxes are not predictive of the changes in jet latitude if moist effects are present.

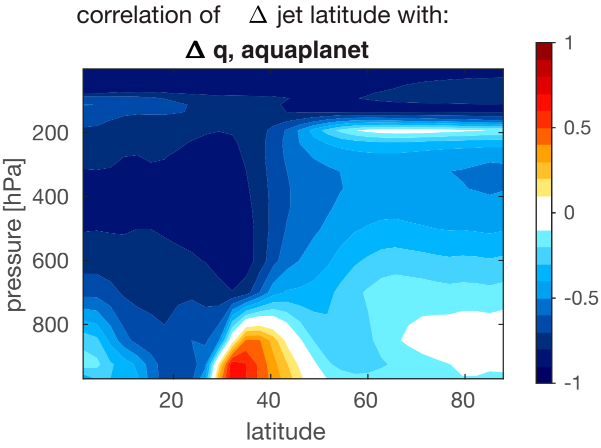

FIG. 12. Correlation across all 10 configurations between the 970 hPa jet shift and Δspecific humidity as a function of latitude and pressure.

These results are of direct relevance to projected jet shifts by CMIP models. Figure 13 is constructed analogously to Fig. 4k, except we contrast the projected jet latitude changes and changes in diabatic heating well poleward of the jet in 13 CMIP6 models (section 2a). The correlation between these metrics is 0.75, which is statistically significant even with a relatively small sample size. While the causality in CMIP6 is difficult to disentangle and the convection scheme used in MiMA is not used by any CMIP6 models to the best of our knowledge, the similarity of the relationship between the CMIP models and the MiMA experiments suggests that the relationships found in our MiMA experiments are relevant to more comprehensive models.

Convective precipitation is available for 32 CMIP6 models for the scenarios considered in Fig. 13, and convective precipitation is related to the vertical integral of convective diabatic heating. We have verified that there is a similar relationship

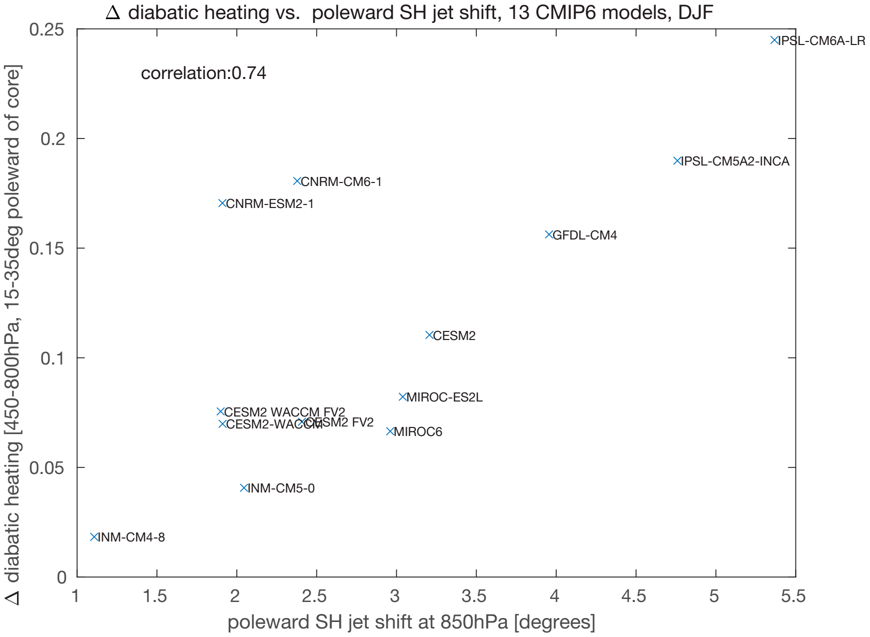

FIG. 13. Comparison of the poleward jet shift at 850 hPa in 13 CMIP6 models listed in Table 1 of Lachmy (2022) in the Southern Hemisphere from December through February (abscissa) to diabatic heating poleward of the jet, defined as the sum of all parameterized heating contributions averaged from 450 to 800 hPa and from 15° to 35° poleward of the jet. The jet latitude is calculated separately for each of the models as the preindustrial control jet latitude ranges by more than 10° among these models. For each model, we computed the climate change response by comparing the last 50 years of the preindustrial control run to the last 50 years of the 4xCO_2 run to focus on the equilibrated response. The requisite data are only available for these 13 models.

to that shown in Fig. 13 for these models, however the correlations are much weaker (0.2); similarly, the correlation of Δ convective precipitation with Δjet latitude in MiMA is 0.5 (cf. Fig. 4j). This weakening of the results when using convective precipitation is not surprising. The vertical distribution of convective heating is important, as increased convective heating in, for example, the boundary layer does not influence the large-scale dynamics in the same way that midtroposphere convective heating does. Our analysis using the temperature budget explains why this is the case. That being said, our results are consistent with Tan and Shaw (2020), who find that differences among models in the projected jet shift are related to differences in the subtropical–subpolar contrast of lower-tropospheric moist static energy.

Several other possible explanations have been offered as to why the magnitude of jet shifts in response to increased GHG differs across models. These explanations include biases in the climatological jet latitude (Kidston and Gerber 2010; Simpson and Polvani 2016; Curtis et al. 2020), differences in the cloud radiative response (Ceppi et al. 2014; Voigt et al. 2019), and differences in the polar stratospheric response (Simpson et al. 2018; Ceppi and Shepherd 2019). Figure 13 supports the recent results of Fuchs et al. (2022) that suggest an additional possibility: differences in the response of convection and convective diabatic heating, particularly poleward of the jet. We hope that future CMIP generations will prioritize vertically resolved diabatic heating, and more specifically convective diabatic heating, as our results suggest that this output may help explain intermodel spread in jet and storm track shifts.

The framework used here for connecting the diabatic heating to the eddy-driven jet latitude is similar to that of Lachmy and Kaspi (2020) and Lachmy (2022), where the diabatic heating is connected to the structure of the Ferrel cell via the heat budget, and the structure of the Ferrel cell is connected to the eddy-driven jet latitude via the momentum budget. The relationship found here between diabatic heating and the jet shift is somewhat different than that found in Lachmy (2022) for CMIP6 models, since the range of latitudes considered for the diabatic heating is different. Lachmy (2022) considered the strength of diabatic heating in the midtroposphere, averaged around its midlatitude maximum. There it was found that the strengthening of midlatitude diabatic heating in response to climate change has a weak negative correlation with the magnitude of the poleward jet shift, and a strong positive correlation with the latitudinal separation between the maximum poleward eddy heat flux and the eddy-driven jet (Figs. 5d,e of Lachmy 2022). While the details of the analysis are different, both the current study and that of Lachmy (2022) connect the response of diabatic heating to climate change with the jet shift, based on the role of diabatic heating in balancing the cooling by the Ferrel cell rising branch, and the connection between the latitudinal structures of the Ferrel cell and the eddy-driven jet.

Changes in jet latitude and in the latitude of the storm track as diagnosed by transient eddy kinetic energy are tightly coupled (Fig. 4a). A similarly tight connection exists between the jet shift and the change in the latitude of the maximum in moist static energy flux (correlation of 0.89 across the 10 configurations included in Fig. 4, not shown). Other Eulerian measures of the storm track are less consistent with the jet shift. For example, dry static energy fluxes poleward of the jet decrease in all configurations (which is dominated by $C_p\overline{v'T'}$ in Figs. 5c,d). Nevertheless, our focus is mainly on the transient eddy kinetic energy which strengthens on the poleward flank of the jet for TLS19 even as the equator-to-pole temperature gradient weakens at lower levels more strongly in this integration (Fig. 2).

These results have implications for projected subtropical drying. While in all configurations, precipitation decreases in an absolute sense somewhere within the subtropics (Fig. 1g), the precise latitude and severity of the most negative precipitation response differs across the configurations: the decrease is farther poleward by nearly 10° and more severe in TLS19. Such a decrease would be of great importance to areas with Mediterranean climates, in which much of the rain falls from the equatorward edge of the wintertime storm track (Seager et al. 2019). Hence these simulations capture uncertainty in future precipitation changes in climatologically dry regions mimicking the intermodel spread in CMIP models (e.g., Garfinkel et al. 2020a; Elbaum et al. 2022), suggesting that uncertainty in the convective parameterization could be contributing to intermodel uncertainty in future subtropical drying.

While the goal of this paper is not to suggest which of the various permutations of shallow_convection, use_CAPE, and RHrelax is most physically justifiable, there are some observational constraints of relevance and related implications for CMIP models. Stephens et al. (2019) and Chen et al. (2021) find that CMIP5 and CMIP6 models generally suffer from too easily triggered convection, as compared to observations, which subsequently leads to too frequent weak convective precipitation and not enough intense precipitation. The TLS19 configuration, which has a stronger poleward shift, appears to perform better in this regard as it has more large-scale tropical precipitation (which is inherently more intense), although we note that model-world convective and large-scale rain do not correspond directly to real-world convective and stratiform rain. If the TLS19 configuration is indeed more physical, this would suggest that models with too much tropical convection (i.e., similar to the JG17 configuration) may underestimate the poleward shift. Regardless of which configuration is more physical, the ratio of convective to large-scale precipitation that is spanned by our configurations mimics the range spanned by CMIP models, and hence is likely of relevance for the spread in the jet shift across CMIP models.

We conclude with a few important caveats. There are no clouds in our model, and hence mechanisms for a poleward shift involving cloud radiative effects are, by construction, missing. Adding clouds could lead to differences in the simulated jet and storm track shifts for these identical settings of the convective parameterization. Similarly, the lack of a dynamic ocean omits the ocean's ability to modify jet and storm track shifts. Future work could focus on transient switch-on simulations in which GHG concentrations are instantaneously increased to better quantify how the changes in the thermodynamic starting points lead to changes in the jet. Further, stationary waves are not present in any simulation in this paper, but are known to drive appreciable moist static energy and momentum fluxes in Earth's atmosphere (Brayshaw et al. 2009; Saulière et al. 2012; Barpanda and Shaw 2017; Garfinkel et al. 2020c) and will change in response to increased GHG (Wills et al. 2019). Preliminary work shows that if stationary waves (following White et al. 2020) are added to the JG17 configuration, the jet does shift poleward in response to increased GHG. Finally, it is not clear why subpolar convective heating should increase more strongly in response to global warming for the TLS19 configuration, and we cannot completely rule out that additional aspects of the TLS19 climatology not considered in this paper render it more sensitive to increased greenhouse gases.

Despite these caveats, our results highlight the key role convection plays in uncertainty in the circulation response to increased GHG. Our results also demonstrate that many of the mechanisms that have been proposed to explain the poleward jet shift fail to explain the sensitivity of the jet shift to the convection parameterization in our experiments, which casts some doubt on their importance more generally. Specifically, our results, together with those of Shaw and Tan (2018) and Shaw (2019), are beginning to form a critical mass of evidence against mechanisms that simply invoke tropical upper-tropospheric warming.

Acknowledgments. CIG and BK acknowledge the support of the Israel Science Foundation (Grant Agreement 1727/21). CIG and EPG are supported by the U.S.-Israel Binational Science Foundation (BSF) Grant 2020316. EPG acknowledges support from the U.S. NSF through Grant OAC-2004572. MJ acknowledges support from the Australian Research Council (ARC) Centre of Excellence for Climate Extremes (CE170100023).

Data availability statement. The version of MiMA used in this study, including the modified source code can be downloaded from https://github.com/ianpwhite/MiMA/releases/tag/MiMA-ThermalForcing-v1.0beta (https://doi.org/10.5281/zenodo.4523199).

REFERENCES

Alexeev, V. A., P. L. Langen, and J. R. Bates, 2005: Polar amplification of surface warming on an aquaplanet in "ghost forcing" experiments without sea ice feedbacks. *Climate Dyn.*, **24**, 655–666, https://doi.org/10.1007/s00382-005-0018-3.

Baldwin, M. P., and D. W. J. Thompson, 2009: A critical comparison of stratosphere-troposphere coupling indices. *Quart. J. Roy. Meteor. Soc.*, **135**, 1661–1672, https://doi.org/10.1002/qj.479.

——, D. B. Stephenson, D. W. J. Thompson, T. J. Dunkerton, A. J. Charlton, and A. O'Neill, 2003: Stratospheric memory and skill of extended-range weather forecasts. *Science*, **301**, 636–640, https://doi.org/10.1126/science.1087143.

Barnes, E. A., and D. L. Hartmann, 2011: Rossby-wave scales, propagation and the variability of eddy-driven jets. *J. Atmos. Sci.*, **68**, 2893–2908, https://doi.org/10.1175/JAS-D-11-039.1.

——, and L. Polvani, 2013: Response of the midlatitude jets, and of their variability, to increased greenhouse gases in the

CMIP5 models. *J. Climate*, **26**, 7117–7135, https://doi.org/10.1175/JCLI-D-12-00536.1.

Barpanda, P., and T. Shaw, 2017: Using the moist static energy budget to understand storm-track shifts across a range of time scales. *J. Atmos. Sci.*, **74**, 2427–2446, https://doi.org/10.1175/JAS-D-17-0022.1.

Bartana, H., C. I. Garfinkel, O. Shamir, and J. Rao, 2022: Projected future changes in equatorial wave spectrum in CMIP6. *Climate Dyn.*, **60**, 3277–3289, https://doi.org/10.1007/s00382-022-06510-y.

Betts, A. K., 1986: A new convective adjustment scheme. Part I: Observational and theoretical basis. *Quart. J. Roy. Meteor. Soc.*, **112**, 677–691, https://doi.org/10.1002/qj.49711247307.

——, and M. J. Miller, 1986: A new convective adjustment scheme. Part II: Single column tests using GATE wave, BOMEX, ATEX and Arctic air-mass data sets. *Quart. J. Roy. Meteor. Soc.*, **112**, 693–709, https://doi.org/10.1002/qj.49711247308.

Brayshaw, D. J., B. Hoskins, and M. Blackburn, 2009: The basic ingredients of the North Atlantic storm track. Part I: Land–sea contrast and orography. *J. Atmos. Sci.*, **66**, 2539–2558, https://doi.org/10.1175/2009JAS3078.1.

Butler, A. H., D. W. Thompson, and R. Heikes, 2010: The steady-state atmospheric circulation response to climate change–like thermal forcings in a simple general circulation model. *J. Climate*, **23**, 3474–3496, https://doi.org/10.1175/2010JCLI3228.1.

Ceppi, P., and T. G. Shepherd, 2019: The role of the stratospheric polar vortex for the austral jet response to greenhouse gas forcing. *Geophys. Res. Lett.*, **46**, 6972–6979, https://doi.org/10.1029/2019GL082883.

——, M. D. Zelinka, and D. L. Hartmann, 2014: The response of the Southern Hemispheric eddy-driven jet to future changes in shortwave radiation in CMIP5. *Geophys. Res. Lett.*, **41**, 3244–3250, https://doi.org/10.1002/2014GL060043.

Chang, E. K., Y. Guo, and X. Xia, 2012: CMIP5 multimodel ensemble projection of storm track change under global warming. *J. Geophys. Res.*, **117**, D23118, https://doi.org/10.1029/2012JD018578.

Chemke, R., and Y. Ming, 2020: Large atmospheric waves will get stronger, while small waves will get weaker by the end of the 21st century. *Geophys. Res. Lett.*, **47**, e2020GL090441, https://doi.org/10.1029/2020GL090441.

——, ——, and J. Yuval, 2022: The intensification of winter mid-latitude storm tracks in the Southern Hemisphere. *Nat. Climate Change*, **12**, 553–557, https://doi.org/10.1038/s41558-022-01368-8.

Chen, D., A. Dai, and A. Hall, 2021: The convective-to-total precipitation ratio and the "drizzling" bias in climate models. *J. Geophys. Res. Atmos.*, **126**, e2020JD034198, https://doi.org/10.1029/2020JD034198.

Chen, G., and I. M. Held, 2007: Phase speed spectra and the recent poleward shift of Southern Hemisphere surface westerlies. *Geophys. Res. Lett.*, **34**, L21805, https://doi.org/10.1029/2007GL031200.

——, J. Lu, and D. M. Frierson, 2008: Phase speed spectra and the latitude of surface westerlies: Interannual variability and global warming trend. *J. Climate*, **21**, 5942–5959, https://doi.org/10.1175/2008JCLI2306.1.

Cohen, J., and Coauthors, 2020: Divergent consensuses on Arctic amplification influence on midlatitude severe winter weather. *Nat. Climate Change*, **10**, 20–29, https://doi.org/10.1038/s41558-019-0662-y.

Curtis, P. E., P. Ceppi, and G. Zappa, 2020: Role of the mean state for the Southern Hemispheric jet stream response to CO_2 forcing in CMIP6 models. *Environ. Res. Lett.*, **15**, 064011, https://doi.org/10.1088/1748-9326/ab8331.

Donohoe, A., K. C. Armour, G. H. Roe, D. S. Battisti, and L. Hahn, 2020: The partitioning of meridional heat transport from the last glacial maximum to CO_2 quadrupling in coupled climate models. *J. Climate*, **33**, 4141–4165, https://doi.org/10.1175/JCLI-D-19-0797.1.

Dwyer, J. G., and P. A. O'Gorman, 2017: Moist formulations of the Eliassen–Palm flux and their connection to the surface westerlies. *J. Atmos. Sci.*, **74**, 513–530, https://doi.org/10.1175/JAS-D-16-0111.1.

Elbaum, E., C. I. Garfinkel, O. Adam, E. Morin, D. Rostkier-Edelstein, and U. Dayan, 2022: Uncertainty in projected changes in precipitation minus evaporation: Dominant role of dynamic circulation changes and weak role for thermodynamic changes. *Geophys. Res. Lett.*, **49**, e2022GL097725, https://doi.org/10.1029/2022GL097725.

Fereday, D., R. Chadwick, J. Knight, and A. A. Scaife, 2018: Atmospheric dynamics is the largest source of uncertainty in future winter European rainfall. *J. Climate*, **31**, 963–977, https://doi.org/10.1175/JCLI-D-17-0048.1.

Frierson, D. M. W., 2007: The dynamics of idealized convection schemes and their effect on the zonally averaged tropical circulation. *J. Atmos. Sci.*, **64**, 1959–1976, https://doi.org/10.1175/JAS3935.1.

——, 2008: Midlatitude static stability in simple and comprehensive general circulation models. *J. Atmos. Sci.*, **65**, 1049–1062, https://doi.org/10.1175/2007JAS2373.1.

——, I. M. Held, and P. Zurita-Gotor, 2006: A gray-radiation aquaplanet moist GCM. Part I: Static stability and eddy scale. *J. Atmos. Sci.*, **63**, 2548–2566, https://doi.org/10.1175/JAS3753.1.

——, ——, and ——, 2007: A gray-radiation aquaplanet moist GCM. Part II: Energy transports in altered climates. *J. Atmos. Sci.*, **64**, 1680–1693, https://doi.org/10.1175/JAS3913.1.

Fuchs, D., S. C. Sherwood, D. Waugh, V. Dixit, M. H. England, Y.-L. Hwong, and O. Geoffroy, 2022: Midlatitude jet position spread linked to atmospheric convective types. *J. Climate*, **36**, 1247–1265, https://doi.org/10.1175/JCLI-D-21-0992.1.

Garfinkel, C. I., D. W. Waugh, and E. Gerber, 2013: Effect of tropospheric jet latitude on coupling between the stratospheric polar vortex and the troposphere. *J. Climate*, **26**, 2077–2095, https://doi.org/10.1175/JCLI-D-12-00301.1.

——, O. Adam, E. Morin, Y. Enzel, E. Elbaum, M. Bartov, D. Rostkier-Edelstein, and U. Dayan, 2020a: The role of zonally averaged climate change in contributing to intermodel spread in CMIP5 predicted local precipitation changes. *J. Climate*, **33**, 1141–1154, https://doi.org/10.1175/JCLI-D-19-0232.1.

——, I. White, E. P. Gerber, and M. Jucker, 2020b: The impact of SST biases in the tropical east Pacific and Agulhas Current region on atmospheric stationary waves in the Southern Hemisphere. *J. Climate*, **33**, 9351–9374, https://doi.org/10.1175/JCLI-D-20-0195.1.

——, I. P. White, E. P. Gerber, M. Jucker, and M. Erez, 2020c: The building blocks of Northern Hemisphere wintertime stationary waves. *J. Climate*, **33**, 5611–5633, https://doi.org/10.1175/JCLI-D-19-0181.1.

——, I. White, E. P. Gerber, S.-W. Son, and M. Jucker, 2023: Stationary waves weaken and delay the near-surface response to stratospheric ozone depletion. *J. Climate*, **36**, 565–583, https://doi.org/10.1175/JCLI-D-21-0874.1.

Gerber, E. P., and S.-W. Son, 2014: Quantifying the summertime response of the austral jet stream and Hadley cell to stratospheric ozone and greenhouse gases. *J. Climate*, **27**, 5538–5559, https://doi.org/10.1175/JCLI-D-13-00539.1.

——, L. M. Polvani, and D. Ancukiewicz, 2008: Annular mode time scales in the Intergovernmental Panel on Climate Change Fourth Assessment Report models. *Geophys. Res. Lett.*, **35**, L22707, https://doi.org/10.1029/2008GL035712.

Ghosh, S., O. Lachmy, and Y. Kaspi, 2024: The role of diabatic heating in the midlatitude atmospheric circulation response to climate change. *J. Climate*, https://doi.org/10.1175/JCLI-D-23-0345.1, in press.

Giorgi, F., and P. Lionello, 2008: Climate change projections for the Mediterranean region. *Global Planet. Change*, **63**, 90–104, https://doi.org/10.1016/j.gloplacha.2007.09.005.

Hall, N. M., B. J. Hoskins, P. J. Valdes, and C. A. Senior, 1994: Storm tracks in a high-resolution GCM with doubled carbon dioxide. *Quart. J. Roy. Meteor. Soc.*, **120**, 1209–1230, https://doi.org/10.1002/qj.49712051905.

Harvey, B., P. Cook, L. Shaffrey, and R. Schiemann, 2020: The response of the Northern Hemisphere storm tracks and jet streams to climate change in the CMIP3, CMIP5, and CMIP6 climate models. *J. Geophys. Res. Atmos.*, **125**, e2020JD032701, https://doi.org/10.1029/2020JD032701.

Held, I. M., 1993: Large-scale dynamics and global warming. *Bull. Amer. Meteor. Soc.*, **74**, 228–242, https://doi.org/10.1175/1520-0477(1993)074<0228:LSDAGW>2.0.CO;2.

——, and B. J. Soden, 2006: Robust responses of the hydrological cycle to global warming. *J. Climate*, **19**, 5686–5699, https://doi.org/10.1175/JCLI3990.1.

Hwang, Y.-T., D. M. Frierson, B. J. Soden, and I. M. Held, 2011: Corrigendum: Corrigendum for Held and Soden (2006). *J. Climate*, **24**, 1559–1560, https://doi.org/10.1175/2010JCLI4045.1.

Iacono, M. J., E. J. Mlawer, S. A. Clough, and J.-J. Morcrette, 2000: Impact of an improved longwave radiation model, RRTM, on the energy budget and thermodynamic properties of the NCAR Community Climate Model, CCM3. *J. Geophys. Res.*, **105**, 14 873–14 890, https://doi.org/10.1029/2000JD900091.

Jucker, M., and E. Gerber, 2017: Untangling the annual cycle of the tropical tropopause layer with an idealized moist model. *J. Climate*, **30**, 7339–7358, https://doi.org/10.1175/JCLI-D-17-0127.1.

Kelley, C., M. Ting, R. Seager, and Y. Kushnir, 2012: Mediterranean precipitation climatology, seasonal cycle, and trend as simulated by CMIP5. *Geophys. Res. Lett.*, **39**, L21703, https://doi.org/10.1029/2012GL053416.

Kidston, J., and E. P. Gerber, 2010: Intermodel variability of the poleward shift of the austral jet stream in the CMIP3 integrations linked to biases in 20th century climatology. *Geophys. Res. Lett.*, **37**, L09708, https://doi.org/10.1029/2010GL042873.

——, and G. K. Vallis, 2012: The relationship between the speed and the latitude of an eddy-driven jet in a stirred barotropic model. *J. Atmos. Sci.*, **69**, 3251–3263, https://doi.org/10.1175/JAS-D-11-0300.1.

——, S. M. Dean, J. A. Renwick, and G. K. Vallis, 2010: A robust increase in the eddy length scale in the simulation of future climates. *Geophys. Res. Lett.*, **37**, L03806, https://doi.org/10.1029/2009GL041615.

——, G. K. Vallis, S. M. Dean, and J. A. Renwick, 2011: Can the increase in the eddy length scale under global warming cause the poleward shift of the jet streams? *J. Climate*, **24**, 3764–3780, https://doi.org/10.1175/2010JCLI3738.1.

Kushner, P. J., I. M. Held, and T. L. Delworth, 2001: Southern Hemisphere atmospheric circulation response to global warming. *J. Climate*, **14**, 2238–2249, https://doi.org/10.1175/1520-0442(2001)014<0001:SHACRT>2.0.CO;2.

Lachmy, O., 2022: The relation between the latitudinal shifts of midlatitude diabatic heating, eddy heat flux, and the eddy-driven jet in CMIP6 models. *J. Geophys. Res. Atmos.*, **127**, e2022JD036556, https://doi.org/10.1029/2022JD036556.

——, and Y. Kaspi, 2020: The role of diabatic heating in Ferrel cell dynamics. *Geophys. Res. Lett.*, **47**, e2020GL090619, https://doi.org/10.1029/2020GL090619.

Lin, J., and Coauthors, 2022: Atmospheric convection. *Atmos.–Ocean*, **60**, 422–476, https://doi.org/10.1080/07055900.2022.2082915.

Lorenz, D. J., 2014: Understanding midlatitude jet variability and change using Rossby wave chromatography: Poleward-shifted jets in response to external forcing. *J. Atmos. Sci.*, **71**, 2370–2389, https://doi.org/10.1175/JAS-D-13-0200.1.

——, and D. L. Hartmann, 2001: Eddy-zonal flow feedback in the Southern Hemisphere. *J. Atmos. Sci.*, **58**, 3312–3327, https://doi.org/10.1175/1520-0469(2001)058<3312:EZFFIT>2.0.CO;2.

——, and E. T. DeWeaver, 2007: Tropopause height and zonal wind response to global warming in the IPCC scenario integrations. *J. Geophys. Res.*, **112**, D10119, https://doi.org/10.1029/2006JD008087.

Lu, J., G. Chen, and D. M. Frierson, 2008: Response of the zonal mean atmospheric circulation to El Niño versus global warming. *J. Climate*, **21**, 5835–5851, https://doi.org/10.1175/2008JCLI2200.1.

Manabe, S., and R. T. Wetherald, 1975: The effects of doubling the CO_2 concentration on the climate of a general circulation model. *J. Atmos. Sci.*, **32**, 3–15, https://doi.org/10.1175/1520-0469(1975)032<0003:TEODTC>2.0.CO;2.

McKenna, C. M., and A. C. Maycock, 2021: Sources of uncertainty in multimodel large ensemble projections of the winter North Atlantic oscillation. *Geophys. Res. Lett.*, **48**, e2021GL093258, https://doi.org/10.1029/2021GL093258.

Merlis, T. M., T. Schneider, S. Bordoni, and I. Eisenman, 2013: Hadley circulation response to orbital precession. Part II: Subtropical continent. *J. Climate*, **26**, 754–771, https://doi.org/10.1175/JCLI-D-12-00149.1.

Mindlin, J., T. G. Shepherd, C. S. Vera, M. Osman, G. Zappa, R. W. Lee, and K. I. Hodges, 2020: Storyline description of Southern Hemisphere midlatitude circulation and precipitation response to greenhouse gas forcing. *Climate Dyn.*, **54**, 4399–4421, https://doi.org/10.1007/s00382-020-05234-1.

Mlawer, E. J., S. J. Taubman, P. D. Brown, M. J. Iacono, and S. A. Clough, 1997: Radiative transfer for inhomogeneous atmospheres: RRTM, a validated correlated-k model for the longwave. *J. Geophys. Res.*, **102**, 16 663–16 682, https://doi.org/10.1029/97JD00237.

Nakamura, H., T. Sampe, Y. Tanimoto, and A. Shimpo, 2004: Observed associations among storm tracks, jet streams and midlatitude oceanic fronts. *Earth's Climate: The Ocean–Atmosphere Interaction. Geophys. Monogr.*, Vol. 147, Amer. Geophys. Union, 329–345.

O'Gorman, P. A., 2010: Understanding the varied response of the extratropical storm tracks to climate change. *Proc. Natl. Acad. Sci. USA*, **107**, 19 176–19 180, https://doi.org/10.1073/pnas.1011547107.

Okajima, S., H. Nakamura, K. Nishii, T. Miyasaka, A. Kuwano-Yoshida, B. Taguchi, M. Mori, and Y. Kosaka, 2018: Mechanisms for the maintenance of the wintertime basin-scale atmospheric response to decadal SST variability in the North

Pacific subarctic frontal zone. *J. Climate*, **31**, 297–315, https://doi.org/10.1175/JCLI-D-17-0200.1.

Polade, S. D., A. Gershunov, D. R. Cayan, M. D. Dettinger, and D. W. Pierce, 2017: Precipitation in a warming world: Assessing projected hydro-climate changes in California and other Mediterranean climate regions. *Sci. Rep.*, **7**, 10783, https://doi.org/10.1038/s41598-017-11285-y.

Randel, W. J., and I. M. Held, 1991: Phase speed spectra of transient eddy fluxes and critical layer absorption. *J. Atmos. Sci.*, **48**, 688–697, https://doi.org/10.1175/1520-0469(1991)048<0688:PSSOTE>2.0.CO;2.

Rio, C., A. D. Del Genio, and F. Hourdin, 2019: Ongoing breakthroughs in convective parameterization. *Curr. Climate Change Rep.*, **5**, 95–111, https://doi.org/10.1007/s40641-019-00127-w.

Rivière, G., 2011: A dynamical interpretation of the poleward shift of the jet streams in global warming scenarios. *J. Atmos. Sci.*, **68**, 1253–1272, https://doi.org/10.1175/2011JAS3641.1.

Saulière, J., D. J. Brayshaw, B. Hoskins, and M. Blackburn, 2012: Further investigation of the impact of idealized continents and SST distributions on the Northern Hemisphere storm tracks. *J. Atmos. Sci.*, **69**, 840–856, https://doi.org/10.1175/JAS-D-11-0113.1.

Seager, R., T. J. Osborn, Y. Kushnir, I. R. Simpson, J. Nakamura, and H. Liu, 2019: Climate variability and change of Mediterranean-type climates. *J. Climate*, **32**, 2887–2915, https://doi.org/10.1175/JCLI-D-18-0472.1.

Shaw, T. A., 2019: Mechanisms of future predicted changes in the zonal mean mid-latitude circulation. *Curr. Climate Change Rep.*, **5**, 345–357, https://doi.org/10.1007/s40641-019-00145-8.

——, and Z. Tan, 2018: Testing latitudinally dependent explanations of the circulation response to increased CO_2 using aquaplanet models. *Geophys. Res. Lett.*, **45**, 9861–9869, https://doi.org/10.1029/2018GL078974.

——, and Coauthors, 2016: Storm track processes and the opposing influences of climate change. *Nat. Geosci.*, **9**, 656–664, https://doi.org/10.1038/ngeo2783.

——, P. Barpanda, and A. Donohoe, 2018: A moist static energy framework for zonal-mean storm-track intensity. *J. Atmos. Sci.*, **75**, 1979–1994, https://doi.org/10.1175/JAS-D-17-0183.1.

——, O. Miyawaki, and A. Donohoe, 2022: Stormier Southern Hemisphere induced by topography and ocean circulation. *Proc. Natl. Acad. Sci. USA*, **119**, e2123512119, https://doi.org/10.1073/pnas.2123512119.

Sigmond, M., P. C. Siegmund, E. Manzini, and H. Kelder, 2004: A simulation of the separate climate effects of middle-atmospheric and tropospheric CO_2 doubling. *J. Climate*, **17**, 2352–2367, https://doi.org/10.1175/1520-0442(2004)017<2352:ASOTSC>2.0.CO;2.

Simpson, I. R., and L. M. Polvani, 2016: Revisiting the relationship between jet position, forced response, and annular mode variability in the southern midlatitudes. *Geophys. Res. Lett.*, **43**, 2896–2903, https://doi.org/10.1002/2016GL067989.

——, T. G. Shepherd, P. Hitchcock, and J. F. Scinocca, 2013: Southern Annular Mode dynamics in observations and models. Part II: Eddy feedbacks. *J. Climate*, **26**, 5220–5241, https://doi.org/10.1175/JCLI-D-12-00495.1.

——, T. A. Shaw, and R. Seager, 2014: A diagnosis of the seasonally and longitudinally varying midlatitude circulation response to global warming. *J. Atmos. Sci.*, **71**, 2489–2515, https://doi.org/10.1175/JAS-D-13-0325.1.

——, P. Hitchcock, R. Seager, Y. Wu, and P. Callaghan, 2018: The downward influence of uncertainty in the Northern Hemisphere stratospheric polar vortex response to climate change. *J. Climate*, **31**, 6371–6391, https://doi.org/10.1175/JCLI-D-18-0041.1.

Stephens, B. A., C. S. Jackson, and B. M. Wagman, 2019: Effect of tropical nonconvective condensation on uncertainty in modeled projections of rainfall. *J. Climate*, **32**, 6571–6588, https://doi.org/10.1175/JCLI-D-18-0833.1.

Swart, N. C., and J. C. Fyfe, 2012: Observed and simulated changes in the Southern Hemisphere surface westerly wind-stress. *Geophys. Res. Lett.*, **39**, L16711, https://doi.org/10.1029/2012GL052810.

Tan, Z., and T. A. Shaw, 2020: Quantifying the impact of wind and surface humidity-induced surface heat exchange on the circulation shift in response to increased CO_2. *Geophys. Res. Lett.*, **47**, e2020GL088053, https://doi.org/10.1029/2020GL088053.

——, O. Lachmy, and T. A. Shaw, 2019: The sensitivity of the jet stream response to climate change to radiative assumptions. *J. Adv. Model. Earth Syst.*, **11**, 934–956, https://doi.org/10.1029/2018MS001492.

Tuel, A., and E. A. B. Eltahir, 2020: Why is the Mediterranean a climate change hot spot? *J. Climate*, **33**, 5829–5843, https://doi.org/10.1175/JCLI-D-19-0910.1.

Vallis, G. K., P. Zurita-Gotor, C. Cairns, and J. Kidston, 2015: Response of the large-scale structure of the atmosphere to global warming. *Quart. J. Roy. Meteor. Soc.*, **141**, 1479–1501, https://doi.org/10.1002/qj.2456.

Voigt, A., N. Albern, and G. Papavasileiou, 2019: The atmospheric pathway of the cloud-radiative impact on the circulation response to global warming: Important and uncertain. *J. Climate*, **32**, 3051–3067, https://doi.org/10.1175/JCLI-D-18-0810.1.

White, I. P., C. I. Garfinkel, E. P. Gerber, M. Jucker, P. Hitchcock, and J. Rao, 2020: The generic nature of the tropospheric response to sudden stratospheric warmings. *J. Climate*, **33**, 5589–5610, https://doi.org/10.1175/JCLI-D-19-0697.1.

Wills, R. C., R. H. White, and X. J. Levine, 2019: Northern Hemisphere stationary waves in a changing climate. *Curr. Climate Change Rep.*, **5**, 372–389, https://doi.org/10.1007/s40641-019-00147-6.

World Meteorological Organization, 1957: Definition of the tropopause. *Bull. WMO*, **6**, 136–137.

Wu, Y., R. Seager, M. Ting, N. Naik, and T. A. Shaw, 2012: Atmospheric circulation response to an instantaneous doubling of carbon dioxide. Part I: Model experiments and transient thermal response in the troposphere. *J. Climate*, **25**, 2862–2879, https://doi.org/10.1175/JCLI-D-11-00284.1.

Yin, J. H., 2005: A consistent poleward shift of the storm tracks in simulations of 21st century climate. *Geophys. Res. Lett.*, **32**, L18701, https://doi.org/10.1029/2005GL023684.

Zappa, G., and T. G. Shepherd, 2017: Storylines of atmospheric circulation change for European regional climate impact assessment. *J. Climate*, **30**, 6561–6577, https://doi.org/10.1175/JCLI-D-16-0807.1.

——, B. J. Hoskins, and T. G. Shepherd, 2015: The dependence of wintertime Mediterranean precipitation on the atmospheric circulation response to climate change. *Environ. Res. Lett.*, **10**, 104012, https://doi.org/10.1088/1748-9326/10/10/104012.

Zhang, X., J. He, J. Zhang, I. Polyakov, R. Gerdes, J. Inoue, and P. Wu, 2013: Enhanced poleward moisture transport and amplified northern high-latitude wetting trend. *Nat. Climate Change*, **3**, 47–51, https://doi.org/10.1038/nclimate1631.